Recognizing Radiation-induced Changes in the Central Nervous System: Where to Look and What to Look For

Masaki Katsura, MD, PhD
Jiro Sato, MD
Masaaki Akahane, MD
Toshihiro Furuta, MD, PhD
Harushi Mori, MD, PhD
Osamu Abe, MD, PhD

Abbreviations: BBB = blood-brain barrier, CNS = central nervous system, RT = radiation therapy

RadioGraphics 2021; 41:224–248

https://doi.org/10.1148/rg.2021200064

Content Codes: MR NR OI RO

From the Department of Radiology, Graduate School of Medicine, The University of Tokyo, 7-3-1 Hongo, Bunkyo, Tokyo 113-8655, Japan (M.K., J.S., T.F., H.M., O.A.); and Department of Radiology, School of Medicine, International University of Health and Welfare, Chiba, Japan (M.A.). Recipient of a Certificate of Merit award for an education exhibit at the 2019 RSNA Annual Meeting. Received April 9, 2020; revision requested May 7 and received May 29; accepted May 30. For this journal-based SA-CME activity, the authors, editor, and reviewers have disclosed no relevant relationships. **Address correspondence to** M.K. (e-mail: *mkatsura-tky@umin.ac.jp*).

SA-CME LEARNING OBJECTIVES

After completing this journal-based SA-CME activity, participants will be able to:

- Describe the pathophysiologic basis of radiation-induced injury and discuss the clinical aspects of radiation-induced neurotoxic effects.
- Discuss the timeline and expected imaging appearances after RT and recognize the characteristic imaging features after RT with concomitant chemotherapy.
- Identify the high-risk features that indicate tumor recurrence and discuss the role of advanced imaging techniques.

See rsna.org/learning-center-rg.

Radiation therapy (RT) continues to play a central role as an effective therapeutic modality for a variety of tumors and vascular malformations in the central nervous system. Although the planning and delivery techniques of RT have evolved substantially during the past few decades, the structures surrounding the target lesion are inevitably exposed to radiation. A wide variety of radiation-induced changes may be observed at posttreatment imaging, which may be confusing when interpreting images. Histopathologically, radiation can have deleterious effects on the vascular endothelial cells as well as on neuroglial cells and their precursors. In addition, radiation induces oxidative stress and inflammation, leading to a cycle of further cellular toxic effects and tissue damage. On the basis of the time of expression, radiation-induced injury can be divided into three phases: acute, early delayed, and late delayed. Acute and early delayed injuries are usually transient and reversible, whereas late delayed injuries are generally irreversible. The authors provide a comprehensive review of the timeline and expected imaging appearances after RT, including the characteristic imaging features after RT with concomitant chemotherapy. Specific topics discussed are imaging features that help distinguish expected posttreatment changes from recurrent disease, followed by a discussion on the role of advanced imaging techniques. Knowledge of the RT plan, the amount of normal structures included, the location of the target lesion, and the amount of time elapsed since RT is highly important at follow-up imaging, and the reporting radiologist should be able to recognize the characteristic imaging features after RT and differentiate these findings from tumor recurrence.

Introduction

Accurate delineation and optimal sparing of organs at risk is one of the most important points in radiation therapy (RT) planning. Organs at risk often discussed in the field of neuroradiology include the following: the brainstem, hippocampus, pituitary gland, optic nerve and chiasm, circle of Willis, cochlea, retina, eye lens, lacrimal glands, salivary glands, thyroid gland, spinal cord, cauda equina, and brachial plexus (1).

The planning and delivery techniques of RT have evolved substantially during the past few decades. Delivery of radiation from various directions and RT planning with high-definition imaging studies enable the shape of the targeted region to conform as tightly as possible to the tumor while reducing the inclusion of normal tissues in the treatment. This development occurred in the form of three-dimensional conformal RT and then with techniques such as intensity-modulated RT (IMRT) and stereotactic RT/radiosurgery

TEACHING POINTS

- In the central nervous system (CNS), the effects of radiation can be roughly divided into effects on vascular endothelial cells and direct effects on neuroglial cells, in particular the oligodendroglial cells.
- On the basis of the time of expression, radiation-induced injury can be divided into three phases: acute, early delayed, and late delayed. Acute and early delayed injuries are usually transient and reversible, whereas late delayed injuries are generally irreversible. To correctly interpret imaging studies, radiologists should maintain familiarity with the expected imaging appearances after RT and carefully distinguish them from tumor recurrence. Keys to recognizing radiation-induced changes at follow-up imaging are knowledge of *(a)* the amount of time elapsed since RT, *(b)* the location of the target lesion, and *(c)* the amount of normal structures included.
- At imaging, radiation-induced leukoencephalopathy is characterized by cerebral white matter high signal intensity on T2-weighted or fluid-attenuated inversion-recovery (FLAIR) images, usually without enhancement or significant mass effect. It typically exhibits diffuse and symmetric involvement after whole-brain RT, with relative sparing of the subcortical U-fiber, corpus callosum, and gray matter. White matter lesions usually develop around the periventricular white matter at the beginning and progress to diffuse white matter changes with varying degrees of cerebral atrophy over months or years.
- Currently, the only method of distinguishing pseudoprogression and true tumor progression is to perform follow-up examinations of the patient because conventional MRI does not allow differentiation of the two conditions. Imaging may be regularly performed at 2–3-month intervals throughout the follow-up period, although the frequency of imaging can be variable across institutions. In clinical practice, the following features can be helpful: *(a)* presence of symptoms and *(b)* methylation status of the *MGMT* gene promoter.
- Prompt diagnosis of radiation-induced spinal cord myelopathy can be difficult because symptoms can vary, and MRI findings are nonspecific and can vary depending on the timing of MRI with respect to radiation exposure. Some imaging features may be useful in incorporating radiation-induced spinal cord myelopathy in the differential diagnosis, such as the longitudinally extensive cord signal intensity pattern corresponding to the radiation field and demonstration of T1-weighted hyperintense marrow signal changes in vertebrae included in the radiation field.

(2). Advancements also occurred with the advent of proton-beam therapy, in which the properties of the proton particle are used to better control the depth at which the RT is delivered (2).

Although advances in RT technology have considerably improved the delivery of radiation, the surrounding structures inevitably receive some radiation, particularly because of the high doses delivered to the targeted tumor. A wide variety of radiation-induced changes may be observed at posttreatment imaging, which may be confusing when interpreting images. As treatment options in oncology continue to expand and long-term survival increases, diagnostic radiologists should maintain familiarity with the expected imaging appearances after RT and carefully distinguish them from tumor recurrence.

In this article, we review the pathophysiologic basis of radiation-induced injury and discuss the timeline and expected imaging appearances after RT, including the characteristic imaging features after RT with concomitant chemotherapy. Special attention is paid to the imaging features that help distinguish expected posttreatment changes from recurrent disease, followed by a discussion on the role of advanced imaging techniques.

Pathophysiology of Radiation-induced Injury

In the central nervous system (CNS), the effects of radiation can be roughly divided into effects on vascular endothelial cells and direct effects on neuroglial cells, in particular the oligodendroglial cells (3). Vascular endothelial damage causes altered permeability, leading to vasogenic edema and disruption of the blood-brain barrier (BBB) or blood–spinal cord barrier. Preclinical studies suggest that endothelial damage may occur within the first 24 hours after irradiation (4). Endothelial damage can lead to other late vascular effects, such as telangiectasia, thrombosis, occlusion of small vessels, fibrinoid deposits, and hyaline thickening of vessel walls (3). As a result, ischemic stroke or hemorrhage may occur months to years after RT (5).

Oligodendrocytes are the most radiosensitive type of glial cell, with cell death occurring rather early after relatively low doses of irradiation (3). Radiation not only reduces the number of mature oligodendrocytes but also induces loss of their precursors, the oligodendrocyte type 2 astrocyte (3). This results in failure to replace normally turned over oligodendrocytes, with the eventual consequence being demyelination.

In addition, there are changes in cellular composition such as increased numbers of reactive astrocytes (gliosis) and microglia (3). These reactive cells have been reported to produce reactive oxygen species, proinflammatory cytokines, and growth factors (eg, vascular endothelial growth factor [VEGF]), leading to a cycle of further cellular toxic effects and tissue damage (3). Increasing evidence from experimental studies has revealed that radiation is cytotoxic to proliferating neuroglial progenitor cells, including neural stem cells, neuronal precursor cells, and glial precursor cells (6). Chronic damage to the progenitor cell populations responsible for hippocampal neurogenesis and white matter integrity may play a major role in late delayed radiation-induced neurotoxic effects, including cognitive impairment and white matter disease (6).

Conventional Multifractionated RT and Stereotactic Techniques

Conventional multifractionated RT refers to repeated administration of small doses of radiation to a relatively large target, as in whole-brain RT or focal (involved-field) RT. To spare normal tissues, shaped radiation beams are aimed from several angles of exposure to intersect at the tumor, providing a much larger absorbed dose there than in the surrounding healthy tissue. The response of tumors to radiation has been largely characterized in terms of factors that influence the ability of radiation to damage DNA and that affect a population of cells in tumors in recovering from such damage (7).

The radiobiologic factors that are critical in determining the net effect of RT on tumors have been referred to as the five *R*'s: repair of sublethal cellular damage, repopulation of tumor cells after irradiation, redistribution of tumor cells into RT-sensitive phases of the cell cycle, reoxygenation of the surviving hypoxic tumor cells, and radiosensitivity of tumor cells (8). Fractionation of the total dose minimizes damage to normal tissues by allowing time for enzymatic repair of DNA damage and maximizes the killing of tumor cells (7). The linear quadratic (LQ) model derives from biologic considerations of how cells could be killed by ionizing radiation and is widely used for isoeffective dose calculation in conventional multifractionated RT (7).

Stereotactic techniques (stereotactic RT/radiosurgery) administer the full calculated dose of radiation to a small precisely defined target in one or a limited number of treatment fractions. This is achieved by using multiple nonparallel radiation beams that converge on the target lesion (9). The full therapeutic dose is limited to the area where all of the beams overlap, while nontarget areas receive much smaller doses from one or a limited number of radiation beams (9). The radiobiologic mechanisms of action of stereotactic RT/radiosurgery have not yet been clearly established (7,10) but appear to differ from those of conventional multifractionated RT.

For stereotactic RT/radiosurgery, the validity and relevance of the classic radiobiologic principles, such as the five *R*'s, have been questioned (7,10). The LQ model has been suggested to overestimate cell death at high-dose hypofractionated stereotactic RT/radiosurgery (10). Emerging evidence indicates that high-dose irradiation used in stereotactic RT/radiosurgery may induce indirect tumor cell death via vascular damage and antitumor immunity, in addition to directly killing tumor cells via DNA damage (10). The controversy regarding the validity of the conventional radiobiologic principles and models for stereotactic RT/radiosurgery highlights the need for further investigations of the biologic mechanisms of stereotactic RT/radiosurgery.

The prerequisites for successful stereotactic RT/radiosurgery include precise delineation of the target using high-definition imaging, an understanding of the anatomy surrounding the lesion, and the technology required to deliver radiation reliably and precisely to the lesion. In stereotactic RT/radiosurgery, the gradient between the high radiation dose delivered to the target volume and the lower dose delivered to peripheral tissues is steep; therefore, accurate spatial registration is essential. However, the surrounding structures may inevitably receive some radiation, particularly because of the high doses delivered to the targeted tumor. Localized or bizarre shapes of radiation-induced injury may be observed at posttreatment imaging, which may be confusing when interpreting images. To correctly interpret imaging studies, the radiologist should be acquainted with the RT delivery technique and RT plan for each patient.

Imaging after RT

On the basis of the time of expression, radiation-induced injury can be divided into three phases: acute, early delayed (Table 1), and late delayed (Table 2) (3). Acute and early delayed injuries are usually transient and reversible, whereas late delayed injuries are generally irreversible (3). To correctly interpret imaging studies, radiologists should maintain familiarity with the expected imaging appearances after RT and carefully distinguish them from tumor recurrence. Keys to recognizing radiation-induced changes at follow-up imaging are knowledge of *(a)* the amount of time elapsed since RT, *(b)* the location of the target lesion, and *(c)* the amount of normal structures included.

Imaging during Acute and Early Delayed Phases

Acute radiation-induced injury in the brain may be expressed as acute radiation encephalopathy in days to weeks after irradiation, particularly in patients with high intracranial pressure. Clinical manifestations of acute radiation encephalopathy include worsening of presenting neurologic symptoms, as well as symptoms and signs of increased intracranial pressure such as nausea, vomiting, drowsiness, and headache (Table 1) (6,11). Symptoms are mostly transient and reversible, although corticosteroids may alleviate them (6,11). Alterations in capillary permeability, disruption of the BBB, and vasogenic edema are thought to be the underlying etiology of acute radiation encephalopathy (11). Imaging appearances at MRI are usually unchanged, but diffuse brain swelling can

Table 1: Radiation-induced Neurotoxic Effects in the Acute and Early Delayed Phases

Anatomic Location	Acute Injury (Days to Weeks after RT)	Early Delayed Injury (1–6 Months after RT)
Brain	Fatigue, headache, anorexia, nausea, and vomiting Worsening of preexisting neurologic symptoms Acute encephalopathy	Fatigue, headache, anorexia, nausea, and vomiting Worsening of preexisting neurologic symptoms Somnolence syndrome Pseudoprogression
Spine	…	Lhermitte sign

Table 2: Radiation-induced Neurotoxic Effects in the Late Delayed Phase

Anatomic Location	Late Delayed Injury (>6 Months after RT)
Brain	Leukoencephalopathy Radiation necrosis Cerebrovascular complications Arteritis (steno-occlusive and moyamoya-like vasculopathy) Intracranial aneurysm Cavernous malformation (hemorrhagic vasculopathy) Strokelike migraine attacks after RT (SMART syndrome) Mineralizing microangiopathy (dystrophic calcification) Chronic expanding encapsulated hematoma Cranial nerve injury Endocrine complications Secondary neoplasms
Spine	Osteoradionecrosis Spinal cord myelopathy Secondary neoplasms

be demonstrated (11). Owing to better understanding of the relationship among dose, schedule, and toxicity, acute radiation encephalopathy is rare with modern treatment techniques.

Early delayed radiation-induced injury in the brain typically occurs 1–6 months after irradiation. Many of the symptoms are similar to those of acute radiation-induced injury, with headache, anorexia, nausea, and vomiting being most frequent. Patients may also present with somnolence, fatigue, transient worsening of preexisting neurologic symptoms, and reversible defects in memory over the course of weeks or months after RT completion (Table 1) (3,6,11).

In addition to vasogenic edema and disruption of the BBB or blood–spinal cord barrier, transient demyelination is thought to be responsible for early delayed radiation-induced injury (3). Spontaneous recovery from symptoms usually occurs within weeks, although corticosteroids are sometimes needed to control signs and symptoms (3). MRI findings can vary from nonenhancing white matter hyperintensity on T2-weighted images (Fig 1) to new or increased size of enhancing lesions in the immediate vicinity of the irradiated tumor volume (11).

If radiation is directed at the spine, a self-limiting early delayed reaction known as the Lhermitte sign is well recognized (Table 1) (3). It occurs after a latent period of 2–4 months after RT and is characterized by an electric shocklike sensation shooting down the spine and extremities during neck flexion (12). The Lhermitte sign after RT is usually followed by a complete clinical recovery after a few months and is not associated with permanent myelopathy (12).

Radiation-induced Leukoencephalopathy

Leukoencephalopathy is generally recognized as a late delayed adverse effect and is thought to develop more than several months after RT. The pathophysiologic mechanisms include damage to oligodendrocytes, thereby causing axonal demyelination and disruption of vascular endothelial cells, leading to coagulative necrosis, vessel thickening, and focal mineralization (13,14).

Radiation-induced leukoencephalopathy may be subclinical, at least initially, although it can result in cognitive deficits consisting of impairments in learning, memory, executive function, attention, and concentration, sometimes developing into dementia and gait disturbance (6,13). Cognitive impairments are common after whole-brain RT (13). Cognitive dysfunction has been suggested to be proportional to the volume and amount of irradiated tissue in the hippocampus dentate gyrus owing to the presence of neural stem cells (6,13). Therefore, sparing of the hippocampus has recently become an important point during the treatment planning process (13,15).

The incidence of radiation-induced leukoencephalopathy varies in previous reports, although it increases with longer follow-up (13). In patients

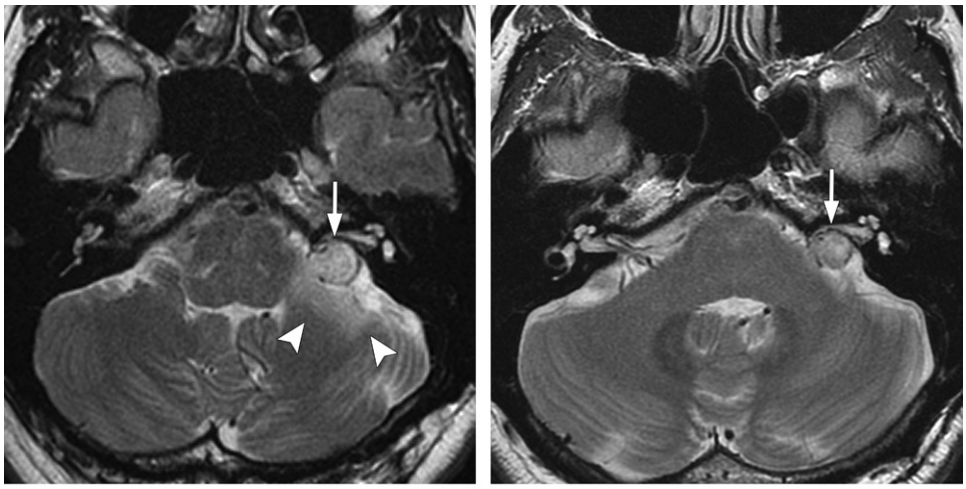

a. b.

Figure 1. Peritumoral edema in a 43-year-old man who underwent stereotactic radiosurgery for a left vestibular schwannoma (arrow). **(a)** Axial T2-weighted MR image 1 month after stereotactic radiosurgery shows peritumoral edema (arrowheads) in the left middle cerebellar peduncle and cerebellar hemisphere. **(b)** Axial T2-weighted MR image 12 months after stereotactic radiosurgery shows spontaneous regression of the peritumoral edema.

who received whole-brain RT for brain metastases, the incidence of radiation-induced leukoencephalopathy was reported to be approximately 30% by 6 months and 100% by 3 years (13). Risk factors related to radiation-induced leukoencephalopathy include higher total dose irradiated, higher dose per fraction, and larger volume of tissue irradiated (6). Use of concurrent or sequential chemotherapy, particularly methotrexate, may significantly increase the incidence and severity of radiation-induced leukoencephalopathy (6).

At imaging, radiation-induced leukoencephalopathy is characterized by cerebral white matter high signal intensity on T2-weighted or fluid-attenuated inversion-recovery (FLAIR) images, usually without enhancement or significant mass effect (6,13,14). It typically exhibits diffuse and symmetric involvement after whole-brain RT, with relative sparing of the subcortical U-fiber, corpus callosum, and gray matter (13). White matter lesions usually develop around the periventricular white matter at the beginning and progress to diffuse white matter changes with varying degrees of cerebral atrophy over months or years (Fig 2) (6,13).

Disseminated Necrotizing Leukoencephalopathy

Disseminated necrotizing leukoencephalopathy (DNL) is an acute and severe form of leukoencephalopathy (16). DNL is a potentially fatal complication of treatment involving intrathecal administration of chemotherapeutic agents such as methotrexate. Direct toxic effects on the oligodendroglia and vascular injury due to endothelial damage have been proposed as the likely mechanisms of methotrexate-related neurotoxic effects (17).

DNL can result from methotrexate therapy alone or in combination with RT. According to Pande et al (17), destruction of the BBB after irradiation and retention of methotrexate may additively or synergistically cause methotrexate to spread more easily through the brain tissue, resulting in necrosis of the deep white matter. In a retrospective study of 143 patients with CNS lymphoma or leukemia treated with intrathecal methotrexate alone or in combination with whole-brain RT, four patients (2.8%) developed DNL (18).

Clinically, DNL is characterized by rapid deterioration of neurologic symptoms after treatment, which can be fatal. The presenting features include personality change, confusion, ataxia, seizures, and coma (16,17). The critical doses and latent periods of both methotrexate and RT leading to DNL vary, but higher doses are more likely to cause DNL (17).

Histologic abnormalities in DNL are observed mainly in the cerebral white matter, with both parenchymal and vascular involvement (14,16–18). Parenchymal changes include multiple foci of coagulative necrosis, demyelination, astrocytic hypertrophy, axonal swelling, and severe status spongiosus (16). Vascular changes include fibrinoid degeneration and hyalinized thickening of the vessel, particularly prominent in venules and capillaries on the venous side (16).

CT demonstrates diffuse usually symmetric low attenuation in the cerebral white matter, although asymmetric involvement has been reported (17). Calcifications progressively increasing in size at the necrotic deep white matter region have been reported in a case of DNL followed up with CT

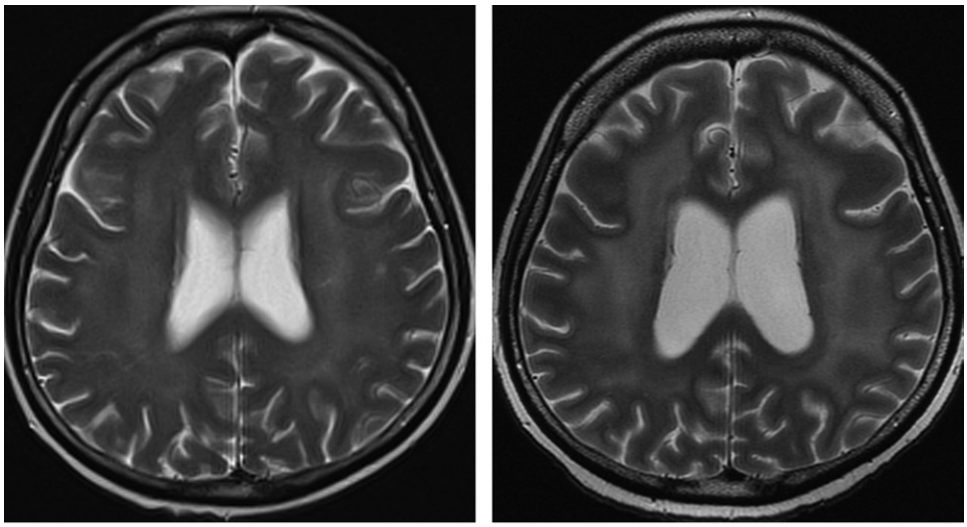

a. b.

Figure 2. Radiation-induced leukoencephalopathy in a 53-year-old woman who received whole-brain radiation therapy (RT) and chemotherapy, including methotrexate, for primary central nervous system (CNS) lymphoma. Axial T2-weighted images 3 months **(a)** and 6 months **(b)** after treatment show symmetric diffuse white matter hyperintensity and atrophy, which progressed over the course.

(17). At MRI, T2-hyperintense areas with small irregular T2 low-signal-intensity foci can be observed in DNL (Fig 3) (16,17). The T2 low-signal-intensity areas are suggestive of vascular damage and coagulative necrosis (16).

The enhancement pattern after administration of contrast material may be patchy or diffuse (Fig 3) (16–18). Restricted diffusion may (18) or may not (17) be observed at diffusion-weighted imaging (Fig 3). Mass effect is uncommon in DNL, although multiple tumorlike lesions with mass effect have been reported (17). Rapid clinical deterioration after treatment is characteristic of DNL, and serial follow-up images may reveal the progression from mild leukoencephalopathy to multifocal necrosis in DNL.

Radiation Necrosis

Cerebral radiation necrosis is a serious late delayed complication that manifests after a latency period of several months, although the range is broad and cases have been reported more than 10 years after irradiation (14,19–21). Histopathologic features of radiation necrosis include fibrinoid changes in the blood vessels, coagulative necrosis, demyelination, and gliosis (14,19). The disruption of the BBB (as visualized on gadolinium-enhanced images) may be mediated in part through vascular endothelial growth factor (VEGF) that is released in response to hypoxia (3).

The reported incidence of radiation necrosis after RT for brain tumors ranges from 3% to 24% (11,19,22). Radiation necrosis is more likely to occur when high doses per fraction are administered, and combined use of chemotherapy with RT may play a role in development of treatment-related necrosis (22). Targeted therapy and immunotherapy may also increase the risk of treatment-related necrosis (23).

Radiation necrosis typically develops at or adjacent to the original site of the tumor, the location that received the highest radiation dose. Radiation necrosis can also develop in part of the normal brain parenchyma that was included in the treatment field of a tumor outside the brain, such as temporal lobe necrosis that develops in some patients treated for a nasopharyngeal cancer (Fig 4) (20). Symptoms produced by localized brain necrosis depend on the location of the lesion and can include focal neurologic deficits or more generalized signs and symptoms of increased intracranial pressure. In many cases, radiation necrosis is a self-limiting process that can be managed conservatively without intervention, although some patients need steroids for symptomatic relief.

Previous reports demonstrated that bevacizumab, an anti-VEGF monoclonal antibody, improves neurologic symptoms and imaging findings in selected cases of cerebral radiation necrosis (24). Symptomatic or radiologic relapse is not uncommon, and some patients require re-treatment with bevacizumab (24). Known adverse effects of bevacizumab are hypertension and cerebral hemorrhage (24). Surgical resection of the necrotic tissue is sometimes required, particularly in cases where there is diagnostic uncertainty as to whether the radiologic changes are indicative of tumor progression or radiation necrosis, or in patients with severe necrosis who have contraindications to bevacizumab such as hemorrhage.

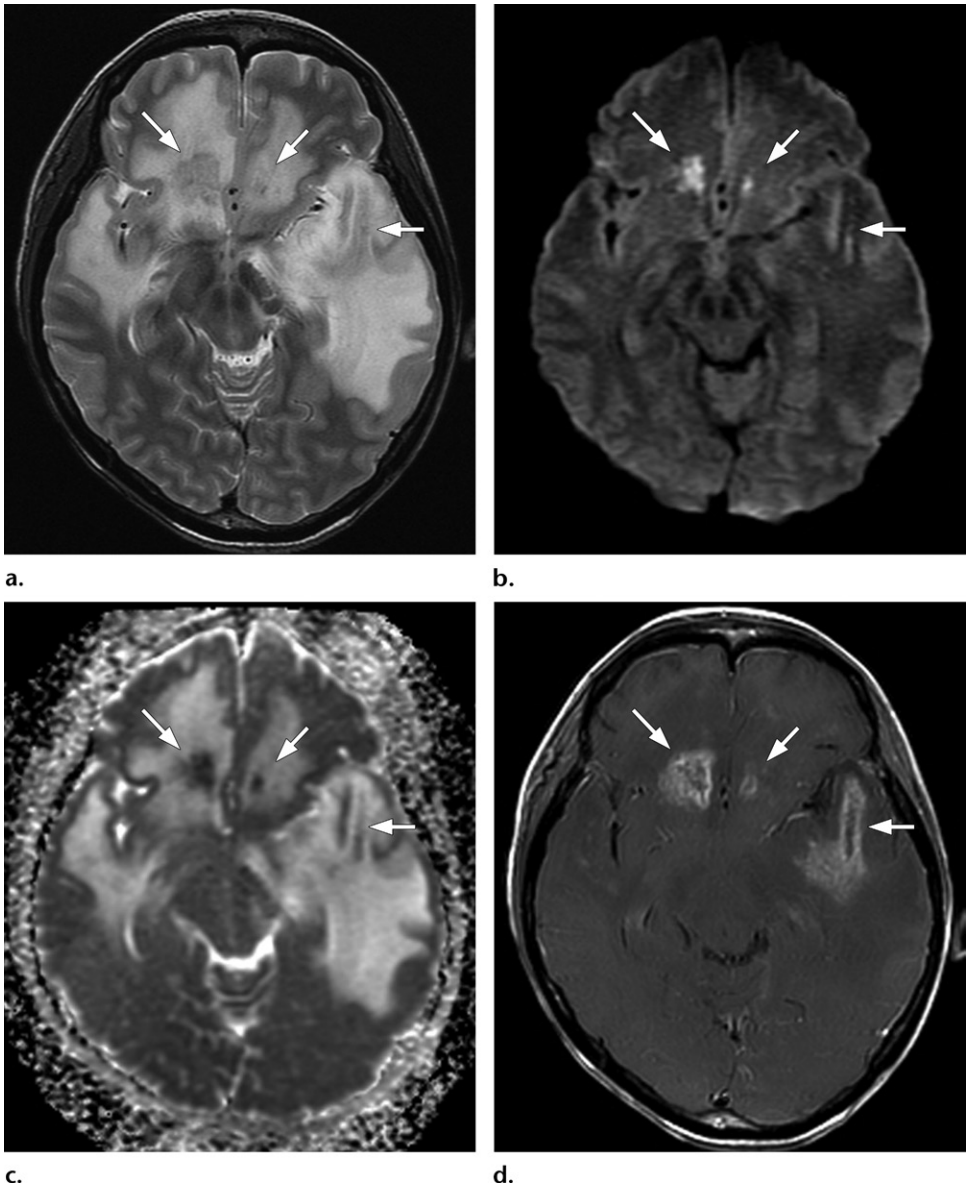

Figure 3. Disseminated necrotizing leukoencephalopathy (DNL) in a 40-year-old woman with primary CNS lymphoma. She presented with changes in behavior, aggression, and memory loss after receiving intrathecal methotrexate and whole-brain RT. **(a)** Axial T2-weighted image shows extensive white matter hyperintensity involving the bilateral frontal and temporal lobes with multiple low-signal-intensity foci (arrows). **(b, c)** The T2-hypointense foci are hyperintense on a diffusion-weighted image (arrows in **b**) and hypointense on an apparent diffusion coefficient (ADC) map (arrows in **c**), consistent with restricted diffusion. **(d)** Axial contrast-enhanced T1-weighted image shows that the T2-hypointense foci have ring enhancement (arrows).

Conventional MRI typically demonstrates an enhancing mass lesion with central necrosis and reactive edema (Fig 4) (19,21,25). The enhancement pattern is often described as "spreading wavefront," meaning that the margins of the enhancement are ill defined (25), or "soap bubble–like" or "Swiss cheese–like," meaning that the enhancing lesion includes central nonenhancing necrotic components of varying size (19). Multiple lesions are possible, and some lesions may develop distant from the original site of the tumor if the distant site was in the radiation field (19,21). Consultation with the radiation oncologist and radiation dose map should be encouraged whenever feasible.

As radiation necrosis progresses with tumor-like growth, it can lead to marked shrinkage of the white matter and cortex and result in focal brain atrophy (19). The periventricular white matter is among the areas most susceptible to radiation necrosis (19). This may be explained by this neuroanatomic region having relatively poor blood supply from long medullary arteries that lack collateral vessels, making it vulnerable

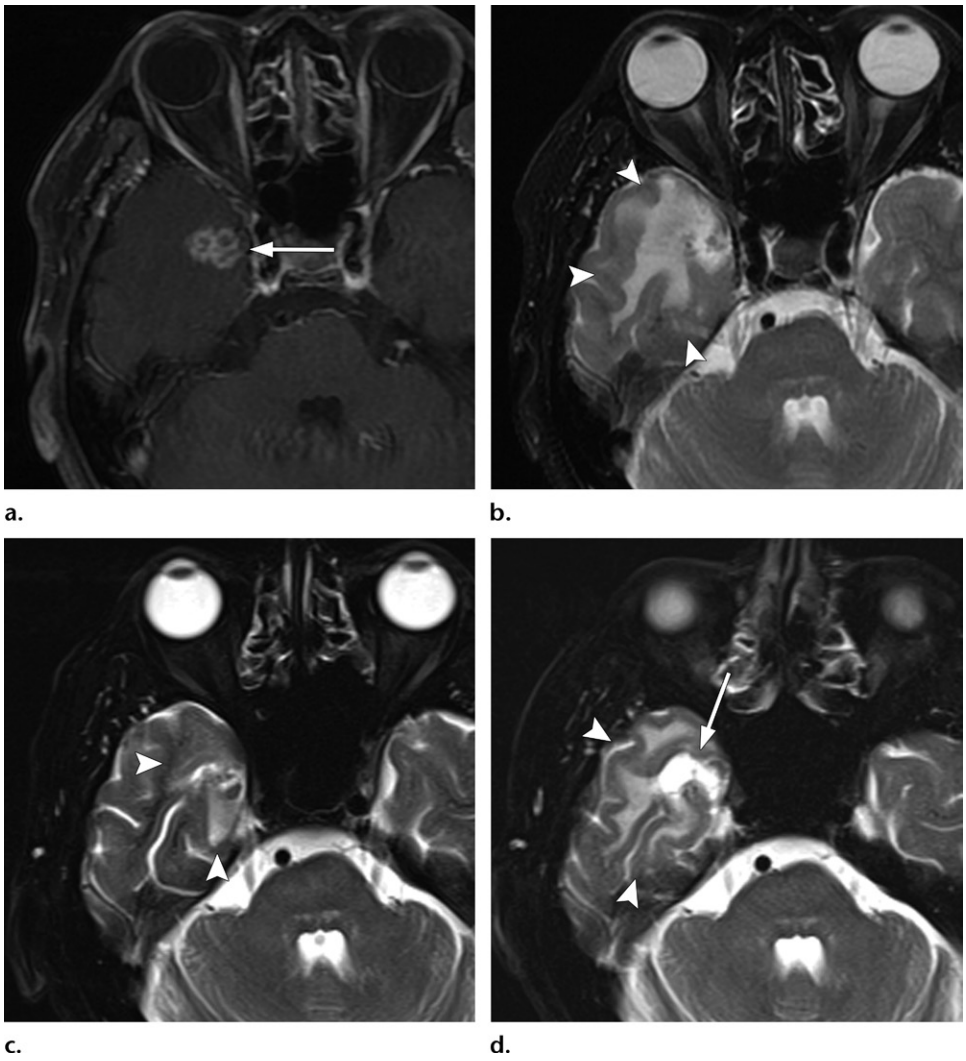

Figure 4. Radiation necrosis in a 57-year-old man who underwent RT (standard-fractionation type) for right-sided nasopharyngeal cancer. **(a)** Axial contrast-enhanced T1-weighted image 5 years after RT shows enhancing foci (arrow) in the right temporal lobe. **(b)** Axial fat-saturated T2-weighted image 5 years after RT shows white matter hyperintensity (arrowheads) surrounding the enhancing lesion. **(c)** Axial fat-saturated T2-weighted image 7 years after RT shows spontaneous regression of the hyperintense white matter lesions (arrowheads). **(d)** Axial fat-saturated T2-weighted image 9 years after RT shows cyst formation (arrow) with increased white matter hyperintensity (arrowheads).

to ischemic effects produced by postirradiation vasculopathy (19).

Imaging findings of radiation necrosis are not always irreversible and progressive but can be static, decrease, or even resolve at follow-up (Fig 4). Wang et al (20) retrospectively analyzed the MRI features of the temporal lobes in 124 patients previously treated with radiation for nasopharyngeal cancer. The appearance and change over time of T2-hyperintense white matter lesions, enhancing lesions, and cysts were assessed.

White matter lesions were the earliest and most common manifestation after RT, followed by enhancing lesions, which often became necrotic with increasing size. Both white matter lesions and enhancing lesions were more likely than cysts to regress, and both could show complete resolution. Cysts were the least frequent pattern of radiation-induced injury and developed from enhancing lesions that exhibited necrosis (Fig 4).

Conventional Imaging for Distinguishing Radiation Necrosis from Tumor Recurrence

Radiologic features of radiation necrosis at conventional imaging overlap with those of recurrent tumors, including high-grade primary brain tumors and brain metastases; therefore, image interpretation can be challenging (19,25). Biopsy of the suspicious lesion may be required for a definitive diagnosis, particularly in patients who are symptomatic and have worsening imaging findings over time. However, it is known that even at histopathologic analysis, residual or recurrent

tumor mixed with radiation necrosis is a common finding (19,22).

Although not always reliable, some clinical or imaging features have been suggested in previous reports and may aid in diagnosis of radiation necrosis and tumor recurrence. First is the time elapsed since RT (21). Radiation necrosis usually manifests after a latency period of many months. Ruben et al (22) investigated 426 glioma patients who underwent RT and reported that the mean interval from the end of RT until the onset of radiation necrosis was 11.6 months (range, 2–32 months), with 67% of cases occurring by 1 year and 85% by 2 years after RT; the actuarial incidence plateaued after 3 years. Although the range can be broad, radiation necrosis typically develops within 2 years after RT in glioma patients, and a new or worsening abnormality starting 3 years after RT is unlikely to be due to pure radiation necrosis (21).

Second is the combined use of MRI patterns. Mullins et al (25) retrospectively reviewed the new enhancing lesions on MR images of 27 patients with high-grade glioma who were treated with proton-beam RT; the findings were compared with the pathologically confirmed diagnosis at subsequent brain biopsy. The MRI features evaluated were corpus callosum involvement, midline spread, subependymal spread, new discrete multiple enhancing foci, "spreading wavefront" appearance, and septum pellucidum involvement.

They reported that none of the individual signs were significant, although combinations of MRI findings yielded statistically significant results. Corpus callosum involvement in conjunction with multiple enhanced lesions—with or without crossing of the midline and subependymal spread—were statistically significant, favoring predominant glioma recurrence. They concluded that combinations of enhancement patterns were more likely than individual patterns to allow distinction of necrosis from predominant tumor progression.

Third is to recognize the common involvement of the temporal lobe after RT for nasopharyngeal cancer (Fig 4). The radiation field for nasopharyngeal cancer includes the skull base, and the inferior and medial aspects of the temporal lobes are often irradiated, which results in an effective radiation dose that exceeds the tolerance limit for neural tissue and leads to a high risk of temporal lobe necrosis (20). The reported incidence of temporal lobe necrosis after intensity-modulated RT (IMRT) for nasopharyngeal cancer varies from 3% to 14% (26). Similarly, the frontal lobes and temporal lobes are often affected by RT for orbital and paranasal or nasal tumors (21). Brain metastases from head and neck malignancies are relatively uncommon compared with those from other primary sites (20).

The latency period for radiation necrosis in patients with nasopharyngeal cancer may vary depending on the fractional dose, overall treatment time, RT technique, size and extension of the primary tumor, and use of chemotherapy (27). In a retrospective analysis of the MRI features of the temporal lobes in 124 patients previously treated with irradiation for nasopharyngeal cancer (20), the median time of first detection after RT of white matter lesions with MRI was 66 months (range, 12–216 months), that for enhancing lesions was 72 months (range, 12–192 months), and that for cysts was 117 months (range, 48–216 months).

Advanced Imaging for Distinguishing Radiation Necrosis from Tumor Recurrence

Several advanced imaging techniques have been investigated in an attempt to differentiate radiation necrosis from tumor recurrence. Diffusion-weighted imaging has been investigated as a potential biomarker of tumor cellularity to differentiate recurrent tumor and necrosis. Restricted diffusion suggests increased cellularity, and low apparent diffusion coefficient (ADC) typically favors the diagnosis of tumor recurrence (Fig 5) (28,29). A recent meta-analysis reported pooled sensitivity of 71% and specificity of 87% for differentiating glioma recurrence from radiation necrosis (30).

However, a high degree of overlap in ADC may exist between the two conditions, particularly when there is viable tumor mixed with necrosis (28,29). Furthermore, the ADC may be influenced by several pathophysiologic processes coexisting in the same lesion, such as liquefactive necrosis, coagulative necrosis, hemorrhage, calcifications, edema, gliosis, fibrosis, and inflammatory infiltrate caused by radiation (28–30). Radiation necrosis with markedly low ADC has been reported (28,29); this is likely due to the high viscosity and cellular composition of the inflammatory infiltrate in early necrosis or secondary to the scarring from gliosis or fibrosis in the lesion in later phases (28,29).

MR spectroscopy attempts to identify tumor recurrence by providing information on metabolic changes. Recurrent brain tumors exhibit high ratios of choline/creatine (Cho/Cr) and choline/*N*-acetylaspartate (Cho/NAA) (Fig 5), whereas radiation necrosis exhibits increased lactate and lipid peaks (31,32). Zhang et al (33) conducted a meta-analysis and reported the pooled sensitivity and specificity of Cho/NAA ratios (88% and 86%,

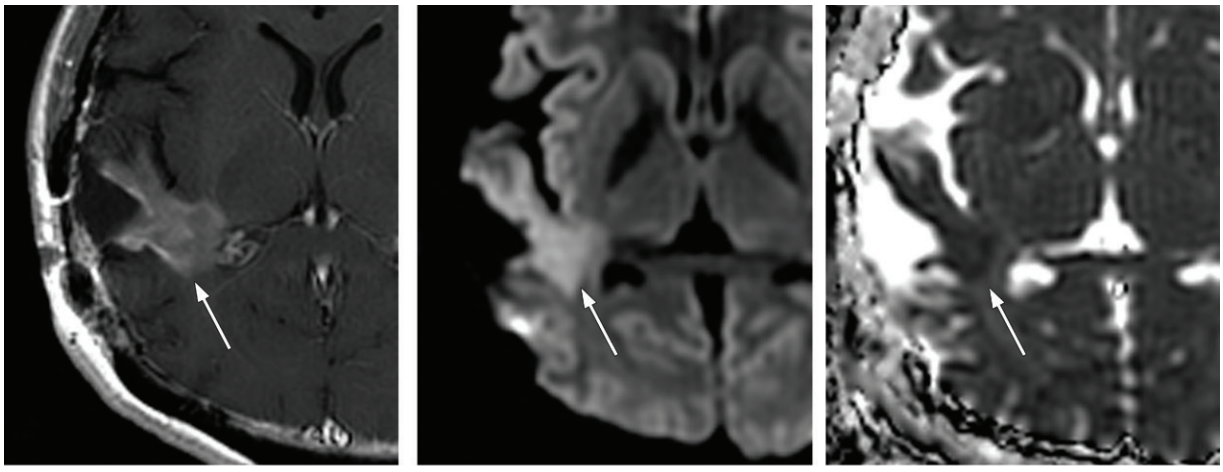

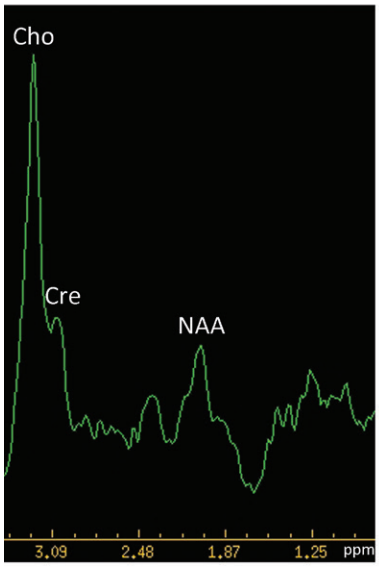

Figure 5. Tumor recurrence in a 27-year-old woman who underwent surgical resection and RT (standard-fractionation type) with temozolomide for anaplastic pleomorphic xanthoastrocytoma in the right temporal lobe 6 months earlier. **(a)** Axial contrast-enhanced T1-weighted image shows an enhancing lesion (arrow) around the resection cavity. **(b, c)** The lesion (arrow) is hyperintense on a diffusion-weighted image **(b)** and hypointense on an apparent diffusion coefficient (ADC) map **(c)**, consistent with restricted diffusion. **(d)** Proton-spectrum image from single-voxel hydrogen 1 MR spectroscopy with echo time of 144 msec shows increased choline/creatine (*Cho*/*Cre*) and choline/*N*-acetylaspartate (*Cho*/*NAA*) ratios. Histopathologic analysis demonstrated tumor recurrence.

respectively) and Cho/Cr ratios (83% and 83%, respectively) for differentiating recurrent glioma from radiation necrosis.

A major problem in comparing different studies on MR spectroscopy is use of different methods to calculate metabolite ratios (32). The utility of MR spectroscopy may be limited in lesions close to the ventricular system or skull because they can yield unreliable measurements owing to signal contamination (30). Surgical clips also disrupt the local field homogeneity and may affect the quality of the data (30). The choice of echo time is also known to have marked effects on detection of certain metabolites (32).

Furthermore, heterogeneous lesions containing tumor tissue and normal or radiation-injured brain tissue are not well evaluated using single-voxel spectroscopy. Single-voxel spectroscopy measures the average metabolite concentration in the chosen image volume, which may result in an inaccurate spectral profile and prevent clear distinction of tumor recurrence from radiation necrosis (32). Single-voxel spectroscopy also has the disadvantages of uncertain ideal voxel location and the possibility of selection bias (32). Both two-dimensional and three-dimensional multivoxel spectroscopy enable sampling of multiple discrete regions, which may be necessary to discern the subtle differences between tumor recurrence and radiation injury and identify areas of both tumor and inflammatory changes in the same enhancing lesion (32).

Dynamic susceptibility contrast (DSC) MRI is the most widely used perfusion technique for brain tumors. DSC perfusion MRI relies on the T2- and T2*-shortening effects of gadolinium-based contrast agents and involves rapid imaging to capture the signal intensity changes due to the first passage of an intravenously administered contrast agent bolus (34). The main parameter derived from DSC MRI in the context of brain tumors is relative cerebral blood volume (rCBV). rCBV is an indirect index of cerebral blood volume, generally calculated relative to region of interest (ROI) values in the contralateral normal white matter (34). Radiation necrosis typically causes hypoperfusion with reduced rCBV (Fig 6), whereas high-grade tumor recurrence results in high rCBV (34).

A recent meta-analysis reported pooled sensitivity of 87% and specificity of 86% for differentiating recurrent high-grade glioma from radiation necrosis (30). However, there is a high degree of overlap between the two conditions because *(a)* there is often viable tumor mixed with necrosis, *(b)* hyperplastic dilated vasculature can

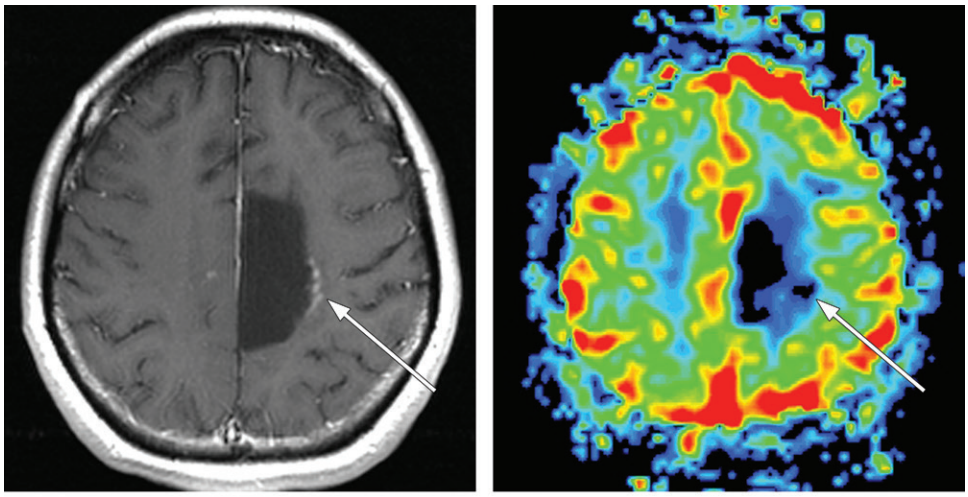

a. b.

Figure 6. Radiation necrosis in a 48-year-old woman with slowly progressive right-sided weakness after surgical resection and RT (standard-fractionation type) for a left parietal lobe astrocytoma. **(a)** Axial contrast-enhanced T1-weighted image shows an enhancing lesion (arrow) around the resection cavity. **(b)** Relative cerebral blood volume (rCBV) map from dynamic susceptibility contrast (DSC) perfusion MRI shows reduced rCBV (arrow).

occur in radiation necrosis, *(c)* BBB disruption with contrast agent leakage interferes with accurate measurement of CBV, and *(d)* the choice of the ROI for "normal white matter" is variable (34). Furthermore, petechial hemorrhage may produce susceptibility artifacts and reduce rCBV values when it occurs in areas of tumor recurrence (34).

Relative peak height (rPH) and percentage of signal recovery (PSR) are two other perfusion parameters that may be derived from DSC MRI. rPH represents the maximum change in signal intensity as contrast agent passes through capillary vascularization (21). The peak value is first calculated by the difference in one ROI before and after contrast agent administration, then a ratio to that of the contralateral normal white matter is calculated (21). rPH has been confirmed to be highly correlated with rCBV and is significantly higher in tumor recurrence than in radiation necrosis (35). Barajas et al (35) found that an rPH cutoff value of 1.38 yielded sensitivity of 89% and specificity of 81% for distinguishing recurrent glioblastoma from radiation necrosis, and rPH values higher than 2.17 were observed only in recurrent tumors.

PSR is determined by comparing the lowest signal intensity during passage of the contrast agent bolus with the end postcontrast signal intensity on the signal intensity–time curve. PSR provides information about contrast agent leakage through the capillary circle, and the relative PSR (rPSR) normalized to that of contralateral white matter is expected to be higher in radiation necrosis than in recurrent tumors (35). Barajas et al (35) found that an rPSR cutoff value of 87.3 yielded sensitivity of 78% and specificity of 76% for distinguishing recurrent glioblastoma from radiation necrosis.

An alternative but less commonly employed perfusion technique is dynamic contrast-enhanced (DCE) MRI, which involves T1-weighted imaging after contrast agent injection over a prolonged period (typically 5 minutes or longer) to assess leakage of contrast agent through the BBB (36,37). For DCE MRI, the vascular volume (CBV) is measured directly without need for a prebolus of contrast agent or correction of the dynamic time series (36,37). The CBV is provided as an absolute figure at DCE MRI; therefore, it is not necessary to normalize the data to the contralateral normal white matter. DCE MRI may also help in cases where DSC images are uninterpretable owing to susceptibility artifact, such as that due to hemorrhage or surgical clips.

In addition to evaluation of blood volume in a lesion, DCE MRI enables assessment of vascular permeability (36,37). The volume transfer constant between blood plasma and the extravascular extracellular space (K_{trans}) is the most commonly used parameter as a measure of vascular permeability, and K_{trans} is often lower in areas of radiation necrosis (36,37), although that quantification is highly dependent on the pharmacokinetic models used (37). A commonly employed scenario is acquisition of DCE images during injection of the preload bolus that is administered in preparation for DSC imaging, although some studies argue that the utility of DCE imaging in common practice is limited (36,37). Zakhari et al (36) prospectively compared the diagnostic accuracy of DCE and DSC imaging

in differentiating tumor recurrence and radiation necrosis in treated high-grade gliomas and found that DSC-derived CBV measurement was more accurate than DCE-derived parameters, including the permeability parameter (K_{trans}).

A noninvasive perfusion MRI technique is arterial spin labeling (ASL), which uses magnetically labeled blood as an endogenous tracer (38). Although its use is not widespread for neuro-oncologic indications, it has several advantages over contrast agent–based perfusion imaging techniques. In patients with poor renal function, difficult intravenous access, and expected long-term follow-up with the risk of gadolinium retention, a noninvasive technique without exogenous contrast agent administration may be preferable (38).

Another advantage of ASL imaging is that cerebral blood flow (CBF) quantification is not affected by contrast agent leakage with BBB disruption (38). Several studies have reported higher CBF in patients with recurrent glioma than in those with radiation necrosis (39). Common artifacts of ASL imaging include motion, signal dropout and distortion resulting from susceptibility effects, bright spots (random clusters of voxels with high perfusion) due to residual vascular signal, and labeling failure of the inflowing blood due to local susceptibility artifacts (38).

Increased uptake with fluorine 18 (^{18}F) fluorodeoxyglucose (FDG) PET suggests tumor, whereas lack of uptake is more suggestive of necrosis (40). However, the utility of ^{18}F-FDG PET may be limited because *(a)* falsely low ^{18}F-FDG uptake can be noted when the recurrent tumor consists mainly of necrosis, *(b)* false-positive findings of recurrent tumor can be caused by increased uptake due to subclinical seizure, *(c)* high uptake in the adjacent normal cortex can reduce sensitivity, and *(d)* many cases of radiation necrosis are actually hypermetabolic (40). The amino acid carbon 11 (^{11}C) methionine can be used for PET and may have advantages over ^{18}F-FDG in distinguishing radiation necrosis from tumor recurrence (41). False-positive findings can be caused by physiologic uptake, anatomic variations, and nontumorous lesions such as inflammation (41).

Pseudoprogression

Pseudoprogression is a subacute treatment-related effect with MRI features mimicking those of tumor progression. Patients can present with an increase in contrast enhancement and peritumoral edema at MRI (Fig 7). The diagnosis of pseudoprogression is typically made retrospectively on the basis of spontaneous improvement or stabilization of imaging findings without intervention (11,42).

Pseudoprogression typically develops in the setting of combined RT and temozolomide therapy for high-grade or low-grade glioma (11) but is also observed with immune checkpoint inhibitors in combination with RT for brain metastases and in cases where chemotherapy-infused wafers were placed in the surgical cavity (23). Pseudoprogression usually develops within 3 months after completion of chemoradiation therapy (CRT) (11) and is often clinically asymptomatic (43). The timing of pseudoprogression is earlier than the typical period in which radiation necrosis is described after RT alone; therefore, it is often classified as an early delayed reaction to radiation (11,22).

Pseudoprogression is most likely induced by a marked local tissue reaction with an inflammatory component, edema, and abnormal vessel permeability causing new or increased enhancement at MRI (11). Pathologically, pseudoprogression is found to correspond to gliosis and reactive radiation-induced changes without evidence of viable tumor (44). Pseudoprogression may represent an exaggerated response to effective therapy, involving early changes to the vascular endothelium and BBB, in addition to oligodendroglial injury leading to inflammation and increased permeability (11). The incidence of pseudoprogression is likely to increase with a higher dose of RT (42).

Furthermore, patients with methylated O^6–methylguanine DNA methyltransferase *(MGMT)* gene promoter demonstrate pseudoprogression more frequently (42). MGMT is a DNA repair enzyme and plays a major role in inducing chemoresistance to temozolomide (11). Tumor cells that are deficient in MGMT (due to methylation of the gene promoter) have increased sensitivity to temozolomide. As mentioned earlier, pseudoprogression may represent an exaggerated response to effective therapy. The higher rates of methylated *MGMT* gene promoter found in patients with pseudoprogression may be correlated with the efficacy of temozolomide CRT on residual tumor burden (11,42).

Among patients with worsened imaging findings at the completion of CRT, approximately 30%–50% have pseudoprogression determined clinically or with biopsy, and the remaining 50%–70% have true tumor progression (43,45,46). Currently, the only method of distinguishing pseudoprogression and true tumor progression is to perform follow-up examinations of the patient because conventional MRI does not allow differentiation of the two conditions (11,42). Imaging may be regularly performed at 2–3-month intervals throughout the follow-up period (43,47), although the frequency of imaging can be variable across

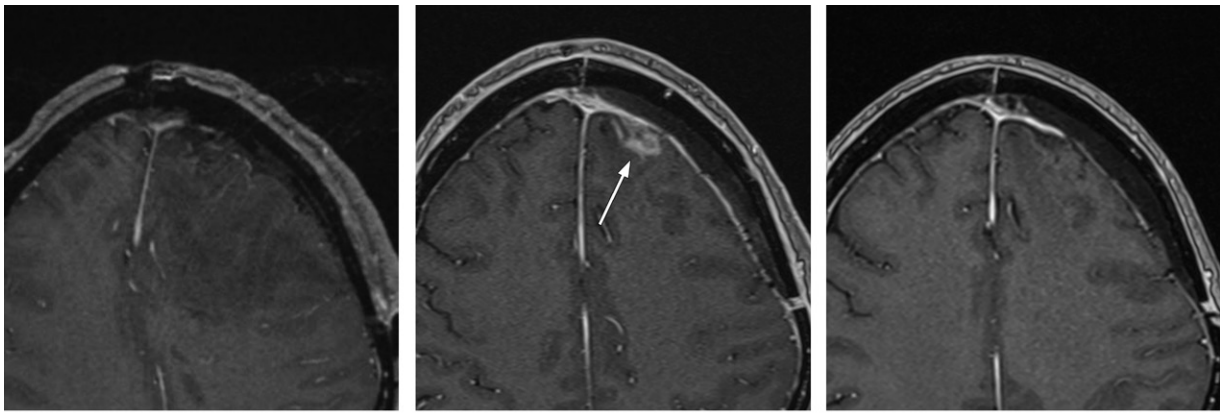

a. b. c.

Figure 7. Pseudoprogression in a 52-year-old woman who received chemoradiation therapy (CRT) (standard-fractionation type) with temozolomide after gross total resection of the enhancing component of a glioblastoma in the left frontal lobe. **(a)** Axial contrast-enhanced T1-weighted image immediately after gross total resection of the tumor. **(b)** Axial contrast-enhanced T1-weighted image 1 month after CRT shows increased enhancement (arrow) around the resection cavity. **(c)** Follow-up image 4 months after CRT shows spontaneous resolution of the lesion.

institutions. In clinical practice, the following features can be helpful: *(a)* presence of symptoms and *(b)* methylation status of the *MGMT* gene promoter.

Pseudoprogression is often asymptomatic (43), whereas true tumor progression is more likely to be associated with clinical decline (46). In one large retrospective series, symptoms were present in 67% of patients with true tumor progression and 33% of those with pseudoprogression (43). The methylation status of the *MGMT* gene promoter has been reported to be an important clinical factor in evaluation of imaging-based changes early in the post-CRT phase of treatment. In a series of 103 patients with newly diagnosed glioblastoma, a 91.3% probability of pseudoprogression in patients with methylated *MGMT* promoter tumors and a 59% probability of true tumor progression in those with unmethylated *MGMT* promoter tumors were described (42).

Several advanced imaging techniques have been investigated in an attempt to distinguish between pseudoprogression and true tumor progression, including diffusion-weighted imaging (48), dynamic susceptibility contrast (DSC) perfusion MRI (44), dynamic contrast-enhanced (DCE) perfusion MRI (49), arterial spin labeling (ASL) imaging (50), and MR spectroscopy (31). However, no single imaging modality has been validated in prospective trials and confirmed to be sufficiently specific to establish a diagnosis (51). The combination of MR spectroscopy and diffusion-weighted imaging and/or perfusion imaging may be powerful (51), but it is important to note that prior studies were relatively small, heterogeneous, and retrospective. Whether these imaging techniques enable reliable distinction between pseudoprogression and true tumor progression needs to be clarified in well-designed prospective series of sufficient size.

The term *pseudoresponse* refers to the phenomenon of tumors appearing to respond to a specific treatment at imaging, when the lesion actually remains stable or has even progressed. The term is largely used in follow-up imaging of high-grade gliomas, in which a rapid decrease in enhancement and edema can be observed in a short period after administration of antiangiogenic agents such as bevacizumab (52). The rapid change can occur within hours of beginning therapy (52). The early decrease in enhancement suggests a change in vascular permeability with "normalization" of the BBB, rather than a true tumor reduction (52). Although use of these medications has been reported to improve progression-free survival, there is no significant effect on overall survival (52,53).

Differentiating pseudoresponse from a true response can be challenging. Follow-up images should always be interpreted with caution after antiangiogenic therapy. Essential to correct interpretation is the availability of multiple previous imaging studies and information relating to the type and timing of therapy. Relying solely on enhancement changes can be misleading, and it is important to pay attention to nonenhancing tumor burden seen on T2-weighted and fluid-attenuated inversion-recovery (FLAIR) images (52). The Response Assessment in Neuro-oncology Working Group proposed that reduced enhancement should persist for at least 4 weeks before being considered to represent a true response (54).

Although restricted diffusion suggests increased cellularity and typically favors the diagnosis of tumor recurrence, this finding can be complicated in the setting of antiangiogenic

therapy. Restricted diffusion often develops at diffusion-weighted imaging after initiation of bevacizumab therapy (55). Histopathologic data from a previous study showed coagulative necrosis and fibrotic hyalinized blood vessels in the regions of restricted diffusion rather than viable tumor (55). Dynamic susceptibility contrast (DSC) perfusion MRI reveals decreased relative cerebral blood volume (rCBV) in areas of previously enhancing tumor (55).

These changes in perfusion metrics may reflect the integrity of the BBB and may not necessarily reflect tumor burden. At MR spectroscopy, increased *N*-acetylaspartate/choline (NAA/Cho) ratios and decreased choline/creatine (Cho/Cr) ratios have been reported in areas of previously enhancing tumor after initiation of therapy and may potentially be useful as an imaging biomarker in assessing response to antiangiogenic treatment (56).

Radiation-induced Arteritis (Steno-occlusive and Moyamoya-like Vasculopathy)

Steno-occlusive vasculopathy of the large cerebral arteries may evolve slowly after irradiation and develops mostly in patients younger than 18 years at the time of RT (57). In a retrospective study of 75 consecutive pediatric patients with primary brain tumors treated with proton RT, the crude incidence of radiation-induced steno-occlusive vasculopathy was approximately 6.7% (58).

The terminal internal carotid artery (ICA) and the major branches of the circle of Willis are especially vulnerable (57,59). In particular, patients with suprasellar or chiasmatic lesions have a high risk for this complication because these tumors often require intense RT near the circle of Willis (59). Omura et al (60) reported that steno-occlusive vasculopathy developed in six (19%) of 32 pediatric patients with primary brain tumors in whom photon radiation fields included the circle of Willis and major cerebral arteries.

Clinical manifestations of radiation-induced steno-occlusive vasculopathy include transient ischemic attacks, infarcts, and seizures (57,59). Histologic studies have revealed subintimal collections of foam cells with myointimal proliferation, which have been broadly characterized as premature or accelerated arteriosclerosis (57). At imaging, there is wall thickening and enhancement of the large cerebral arteries, resulting in a stenotic or occlusive state (Fig 8) (61). Most frequently, terminal parts of the ICA and its branches (eg, middle cerebral artery) are involved, and multivessel involvement is common (57,59).

Furthermore, moyamoya-like collateral circulation and transdural anastomoses may be observed (Fig 8) (57,59,61). Risk factors for developing radiation-induced moyamoya-like vasculopathy include young age at time of RT, high radiation dose, combined chemotherapy, and comorbid neurofibromatosis type 1 (NF1) (59). In a review of 345 children treated with RT for a primary brain tumor, 12 patients (3.5%) developed evidence of moyamoya-like vasculopathy (59).

This study also found that the onset of moyamoya-like vasculopathy was more rapid in patients with NF1 and those who received more than 50 Gy of radiation to the optic chiasm (59). Children with NF1 treated for optic pathway glioma have a high risk for radiation-induced moyamoya-like vasculopathy and may develop this vasculopathy earlier than nonneurofibromatosis patients or after lower radiation exposure (59). The risk of infarction has been reported to be higher in patients with radiation-induced moyamoya-like vasculopathy than in those with idiopathic moyamoya disease (57,59).

Radiation-induced Intracranial Aneurysm

Radiation-induced intracranial aneurysms are a rare but potentially fatal complication of RT and may develop in a wide age group (62). They may be discovered at routine radiologic follow-up or found incidentally after workup for other symptoms. Nanney et al (62) reviewed a series of 46 patients irradiated for various tumors who developed 69 intracranial aneurysms within the irradiated fields over a median period of 12 years. The lag time between RT and diagnosis can be shorter in patients older than 40 years (62), although this may be explained by an overdiagnosis bias wherein people older than 40 years are subject to more follow-up diagnostic procedures. The lag time between RT and diagnosis can be shorter in stereotactic radiosurgery, which may be due to the high-energy focused radiation received by a vessel during the procedure (62).

The pathogenesis of radiation-induced aneurysms is still speculative. However, injuries to endothelial cells, ground substance, elastic lamina, and smooth muscle of the involved vessels have been proposed as primary pathogenic mechanisms (62). Accelerated atherosclerosis secondary to irradiation may also be responsible for aneurysm formation (62). At imaging, radiation-induced intracranial aneurysms are more likely to be saccular (Fig 9) (62). There is a higher incidence in the anterior circulation, and the incidence of multiple aneurysms in a single patient is high (62).

It has been suggested that radiation-induced aneurysms originate directly from the arterial wall

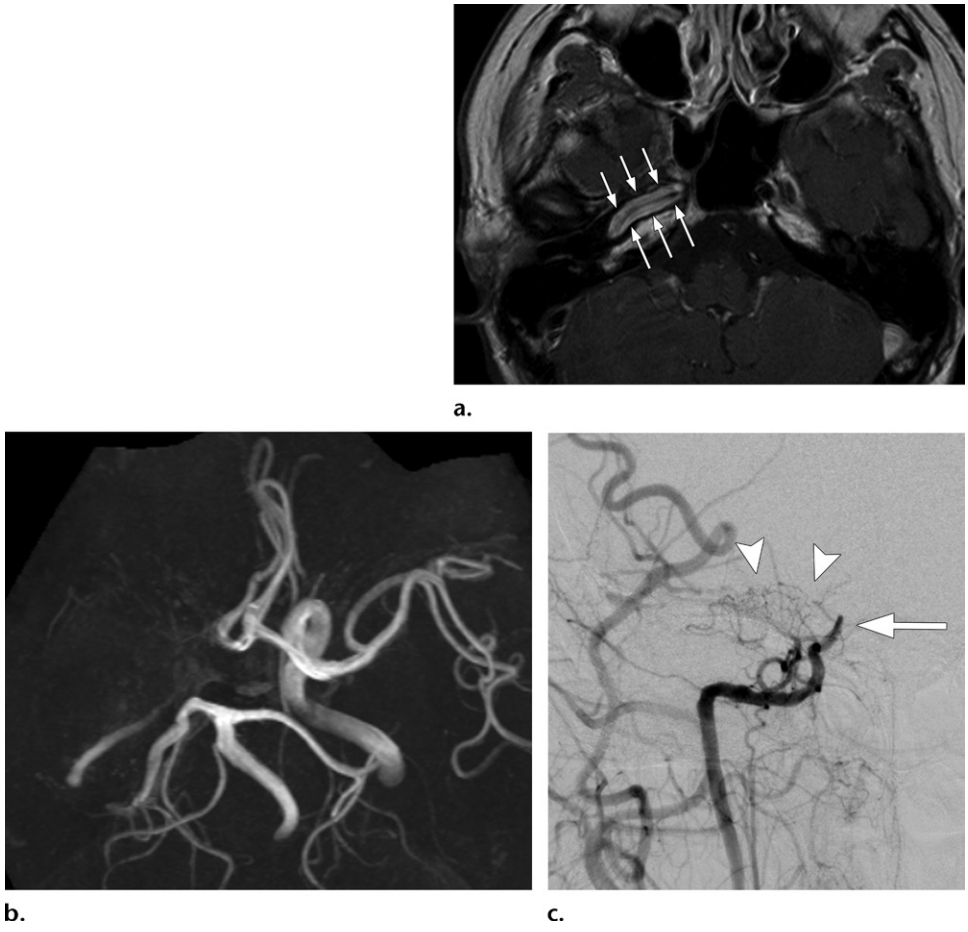

Figure 8. Steno-occlusive vasculopathy in a 47-year-old woman with a history of stereotactic radiosurgery for an arteriovenous malformation in the right temporal lobe. **(a)** Axial contrast-enhanced T1-weighted image shows wall thickening and enhancement of the skull base right internal carotid artery (ICA) (arrows). **(b)** Maximum intensity projection from time-of-flight MR angiography shows the steno-occlusive state of the right distal ICA. **(c)** Frontal projection from digital subtraction angiography of the right ICA shows the steno-occlusive state of the right distal ICA (arrow) and the development of lenticulostriate collaterals at the skull base (arrowheads).

rather than from a branching site like ordinary saccular aneurysms (62). This uncommon location may be related to vessel wall degradation caused by radiation (62). Combined with weakening of the vessel wall by the effects of radiation, the constant shear pressure may precipitate changes that lead to formation of saccular and fusiform aneurysms, pseudoaneurysms, and eventually rupture (62). The reported frequency of rupture is much greater than that expected for non–radiation-induced aneurysms (62), although selection bias may have resulted in a reduced likelihood to report unruptured aneurysms and an increased tendency to report ruptured aneurysms.

Radiation-induced Cavernous Malformations (Hemorrhagic Vasculopathy)

RT is related to development of cavernous malformations in the CNS (63). The cumulative incidence of cerebral cavernous malformations after RT is approximately 3%–4% at 10 years, 7%–14% at 20 years, and possibly as high as 60% at 25 years (64). Radiation-induced cavernous malformations develop more commonly in pediatric patients than in adult patients (63,65). Patients aged 10 years or younger at time of RT have shorter latency and increased incidence of cavernous malformation (65). Previous studies demonstrated a correlation between radiation dose greater than 30 Gy and shorter latency to development of cavernous malformations (65). Spinal cord cavernous malformations after irradiation are rare but have been reported (63).

The underlying mechanism of development of cavernous malformations in response to radiation probably involves vascular injury. Radiation produces endothelial proliferation with hyalinization and fibrinoid necrosis of the vessel walls, then finally ischemia and infarction due to narrowing of the vascular lumen (65). Ischemia activates hypoxia-inducible factor 1 (HIF-1), which in turn in-

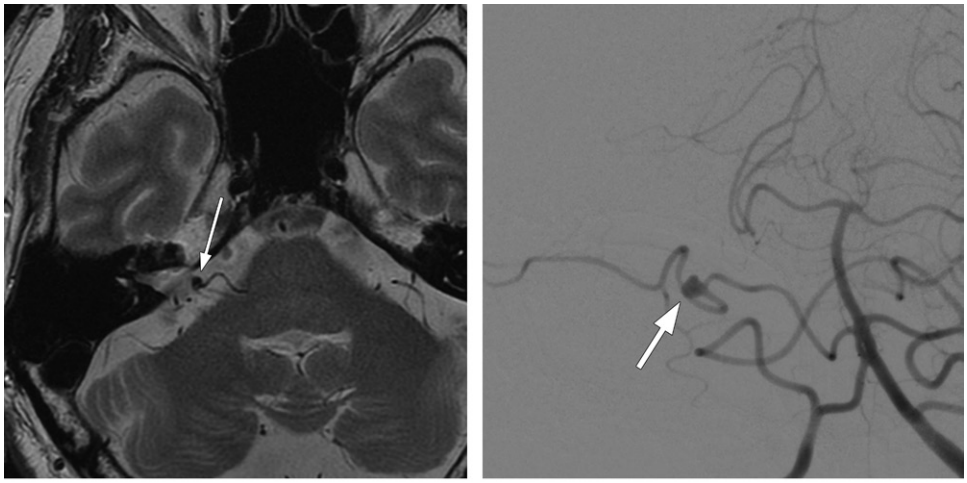

a. b.

Figure 9. Intracranial aneurysm in a 67-year-old man who underwent stereotactic radiosurgery for a right vestibular schwannoma in the right internal auditory canal. Axial T2-weighted image **(a)** and frontal projection from digital subtraction arteriography of the vertebral artery **(b)** 9 years later show a saccular aneurysm (arrow) of the right anterior inferior cerebellar artery.

duces vascular endothelial growth factor (VEGF), generating reactive angiogenesis (65). Expression of these factors decreases with age (65), suggesting that the origin of acquired cavernous malformation is more frequent in early ages.

MRI usually demonstrates a reticulated core of heterogeneous signal intensity on T2-weighted images with a dark peripheral rim of hemosiderin (63). Cavernous malformations can be detected as multiple hypointense lesions on T2*-weighted images (5) and are better detected with susceptibility-weighted imaging (Fig 10) (66). Some lesions may increase in size over time (63). Compared with non–radiation-induced cavernous malformations, radiation-induced cavernous malformations are more likely to occur as multiple lesions and to manifest at a younger age and are at least as likely to cause symptomatic hemorrhage (63).

Strokelike Migraine Attacks after RT (SMART Syndrome)

SMART syndrome, an acronym for strokelike migraine attacks after RT, is an uncommon delayed complication of cranial irradiation. Patients usually present years after RT with migraine-like headaches, seizures, and subacute strokelike episodes with symptoms such as hemiplegia, aphasia, and hemianopia (67). Attacks are typically subacute in onset and resolve after weeks in most cases (67). Although the exact mechanism of SMART syndrome is unknown, the process seems to be driven by cerebral hyperexcitability with impaired autoregulatory mechanisms and vascular endothelial damage as a consequence of remote irradiation (67).

Radiology reports regarding imaging features of SMART syndrome mostly consist of single-case or small-series reports (67–69). Characteristic imaging findings include transient, unilateral, gyriform abnormal T2 and fluid-attenuated inversion-recovery (FLAIR) signal intensity with mild mass effect and cortical enhancement with minimal leptomeningeal enhancement, usually in an area included in the radiation ports (67). Diffusion restriction is variably seen (67). Black et al (67) reported that five (45%) of 11 patients with SMART syndrome had various degrees of multiple magnetic susceptibility foci most compatible with cavernous malformations, probably a consequence of prior RT. Imaging findings may appear 2–7 days after onset of symptoms and typically resolve in 2–5 weeks (67).

In one case series, permanent imaging sequelae from SMART syndrome were demonstrated, with features of cortical laminar necrosis developing as early as 17 days after symptom onset (67). The combination of radiation-induced vascular damage and clinical and subclinical seizure activity could explain cortical edema and impaired BBB integrity with persisting contrast enhancement for days to weeks and, at times, becoming permanent with evidence of cortical laminar necrosis (67). For appropriate diagnosis of SMART syndrome and distinguishing it from recurrent tumor or subacute infarction, it is important for radiologists to be aware of the characteristic imaging findings of SMART syndrome as well as their temporal evolution, the association with seizures, and the possibility of permanent sequelae.

Mineralizing Microangiopathy (Dystrophic Calcification)

Mineralizing microangiopathy with dystrophic calcification is a distinctive histopathologic

process involving the microvasculature of the CNS (70). It usually develops after combined CNS irradiation and chemotherapy in childhood, although it may develop after RT alone (14,70). In an autopsy study of children with leukemia treated with cranial irradiation, mineralizing microangiopathy was detected in 28 (17%) of 163 patients and as early as 10 months after completion of RT (71).

Histologically, the calcification found in mineralizing microangiopathy is present in the walls of precapillary arterioles, capillaries, venules, and smaller arteries such as the lenticulostriate artery (70). Dystrophic calcification also develops in the perivascular neural tissue secondary to mineralization of plasma fluids, which leak out of the damaged vessels, and regional ischemia resulting from circulatory impairment (70). The age of the patient at the time of CNS irradiation may play a significant role in development of mineralizing microangiopathy, and the risk of this complication is greater in children less than 10 years of age who have undergone RT (70).

CT typically demonstrates multiple punctate foci of calcification, predominantly involving the basal ganglia and subcortical white matter (Fig 11) (70). Calcification may also be present in the cerebellar structures and brainstem (14,70). At MRI, the areas of calcification may demonstrate paradoxical hyperintensity on T1-weighted images and hypointensity on T2-weighted images, which can be attributed to a surface-relaxation mechanism associated with particulate calcium (70). It is unclear whether these lesions correlate with clinical symptoms (70). In most cases, mineralizing microangiopathy is asymptomatic and is an incidental finding at follow-up CT (14,70).

Chronic Expanding Encapsulated Hematoma

Cysts and chronic expanding encapsulated hematomas can be observed as late delayed complications after stereotactic radiosurgery for arteriovenous malformations (72,73). Increased permeability of blood vessels of the nidus, BBB breakdown, and liquefaction of coagulation necrosis have been suggested as the cause (72). Shuto et al (72) documented that cysts and chronic expanding encapsulated hematomas are caused by repeated minor hemorrhages from a nodular angiomatous lesion developing within the brain parenchyma adjacent to the irradiated nidus. If the hemorrhage from an angiomatous lesion spreads mainly into the brain parenchyma, a cyst develops and enlarges (72). On the other hand, if the hemorrhage occurs mainly within the angiomatous lesion, a so-called chronic expanding encapsulated hematoma develops (72).

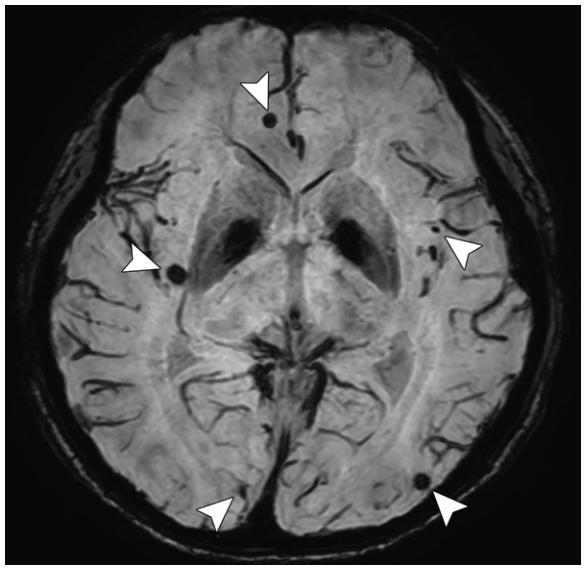

Figure 10. Radiation-induced cavernous malformations in a 37-year-old man who underwent whole-brain RT for acute lymphoblastic leukemia during childhood. Axial susceptibility-weighted image shows multiple low-signal-intensity foci (arrowheads).

Cysts and chronic expanding encapsulated hematomas typically develop more than 2 years after stereotactic radiosurgery (72,73). Hasegawa et al (73) reported that the actuarial incidence of cyst formation or chronic expanding encapsulated hematoma was 1.2%, 5.2%, and 6.3% at 5, 10, and 15 years, respectively, with median interval to progression of 9.4 years. Large nidus volume is the most significant risk factor for developing cysts and chronic expanding encapsulated hematoma (73).

The typical imaging pattern of chronic expanding encapsulated hematoma is a low-signal-intensity or mixed-signal-intensity nodule on T2-weighted images with or without a cyst (Fig 12) (72,73). Destruction of the BBB results in enhancement. The cysts can be multilobulated and are often accompanied by perilesion edema. A fluid-fluid level with different signal intensities within the cyst may be observed owing to multiple hemorrhages with different stages (72). Cysts and chronic expanding encapsulated hematomas may increase in size during follow-up and become symptomatic secondary to mass effect, which can ultimately necessitate surgical intervention (72,73). Symptomatic cysts can be indicated for insertion of an Ommaya reservoir to aspirate the contents repeatedly or a cystoperitoneal shunt (72).

Radiation-induced Cranial Neuropathy

Radiation-induced injury to a cranial nerve is an uncommon late delayed complication of RT for intracranial and extracranial tumors. Radiation damage to the optic nerve or chiasm may

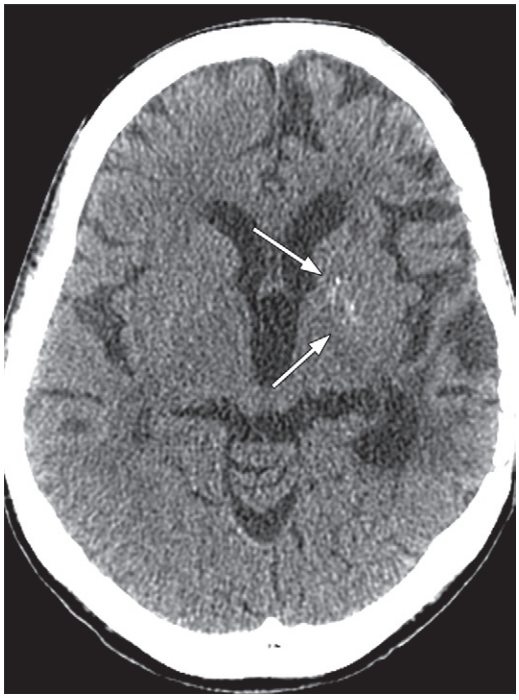

Figure 11. Mineralizing microangiopathy (dystrophic calcification) in a 49-year-old man who underwent focal irradiation (standard-fractionation type) after surgical resection of a left temporal lobe glioma. Axial CT image shows punctate areas of calcifications (arrows) in the left basal ganglia.

develop after whole-brain RT or focal RT for tumors in sites near the visual apparatus, including the pituitary gland, cavernous sinus, orbit, paranasal sinuses, nasal cavity, and nasopharynx (74). Diplopia due to radiation damage to the oculomotor cranial nerves has been infrequently reported after RT for pituitary tumors and skull base tumors (Fig 13) (75). Facial numbness due to radiation damage to the trigeminal nerve may develop after RT for cavernous sinus tumors (76) or essential trigeminal neuralgia (77). Glossopharyngeal, vagus, accessory, and hypoglossal nerve palsies may develop years after RT for head and neck cancer (78).

Histopathologically, radiation-induced cranial nerve injury is thought to be caused by loss of the nerve-blood barrier, demyelination, ischemia, coagulation necrosis, and fibrosis (79). Regarding the lower cranial nerves, radiation-induced cranial neuropathy is thought to be caused by tissue fibrosis with entrapment of nerve trunks, especially in the nerves that course through the neck muscles (78). Total radiation dose, fraction size, and use of chemotherapy greatly affect the incidence of radiation-induced cranial nerve injury (78). The latent period from RT to the onset of clinical symptoms is usually on a scale of years, and long-term follow-up is required to fully understand the cause-and-effect relationship between treatment and its complications.

Radiology reports regarding imaging features of radiation-induced cranial neuropathy mostly consist of single-case or small-series reports, and radiation-induced optic neuropathy is the best documented. The incidence of radiation-induced optic neuropathy has ranged from 0.5% to 9.0%, depending on the size and location of the primary tumor (74). At MRI, radiation-induced optic neuropathy may demonstrate smooth thickening of the affected nerves with enhancement (74,79). Enhancement may precede symptoms and can persist for months after the onset of symptoms (74). Intraorbital enhancement is rare but has been reported (74). Atrophy of the affected nerve may become evident with follow-up (74).

In clinical practice, balanced steady-state free-precession sequences—such as fast imaging employing steady-state acquisition (FIESTA) (General Electric, Milwaukee, Wis) and constructive interference steady-state (CISS) imaging (Siemens Healthineers, Erlangen, Germany)—are essential for depicting the anatomic details of cranial nerves (Fig 13). The possibility of tumor infiltration should always be excluded, including local recurrence, leptomeningeal dissemination, neoplastic meningitis, and perineural spread of malignancy (79,80).

Radiation-induced Endocrinopathy (Hypopituitarism)

Irreversible and progressive radiation-induced neuroendocrine dysfunction, particularly anterior hypopituitarism, is a late-onset sequel of cranial irradiation (81). The hypothalamopituitary axis is frequently included within the irradiation field used for treatment of pituitary and nonpituitary tumors, including primary brain tumors, nasopharyngeal tumors, tumors of the skull base, CNS prophylaxis in patients with acute lymphoblastic leukemia, and total body irradiation before bone marrow transplantation (81). In a systematic review that included 18 studies of long-term endocrine function in adults who had undergone cranial irradiation for primary nonpituitary tumors, the prevalence of any degree of hypopituitarism was 66% (82).

The frequency, speed of onset, and severity of radiation-induced neuroendocrine dysfunction correlate with the total radiation dose delivered to the hypothalamopituitary axis, in addition to the fraction size, younger age at irradiation, and prior pituitary compromise by the tumor and surgery (81). The time course of endocrine dysfunction is variable, with patients typically having abnormal serum hormone levels long before clinical symptoms develop. Abnormalities can develop as early

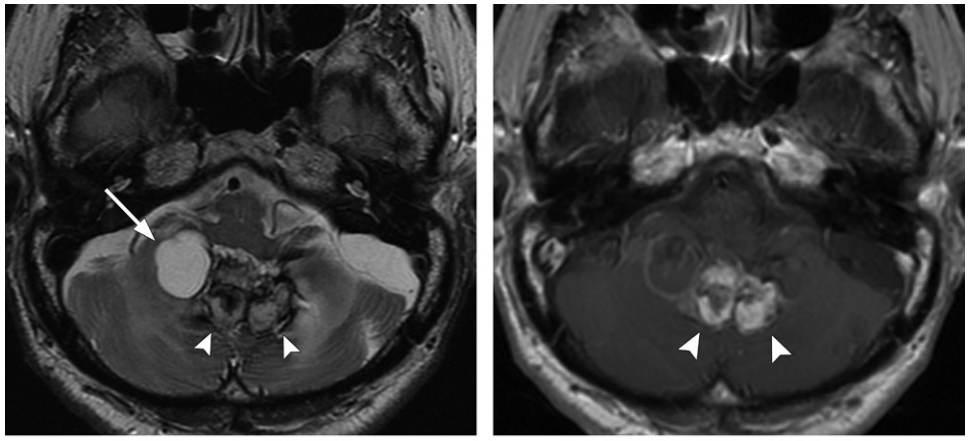

a. b.

Figure 12. Chronic expanding encapsulated hematoma in a 75-year-old man who underwent stereotactic radiosurgery for a cerebellar arteriovenous malformation 24 years earlier. **(a)** Axial T2-weighted image shows a cyst (arrow), a chronic hematoma with superficial siderosis (arrowheads), and perilesion edema in the irradiated area. **(b)** Axial contrast-enhanced T1-weighted image shows disruption of the blood-brain barrier (BBB) within the hematoma as enhancement (arrowheads).

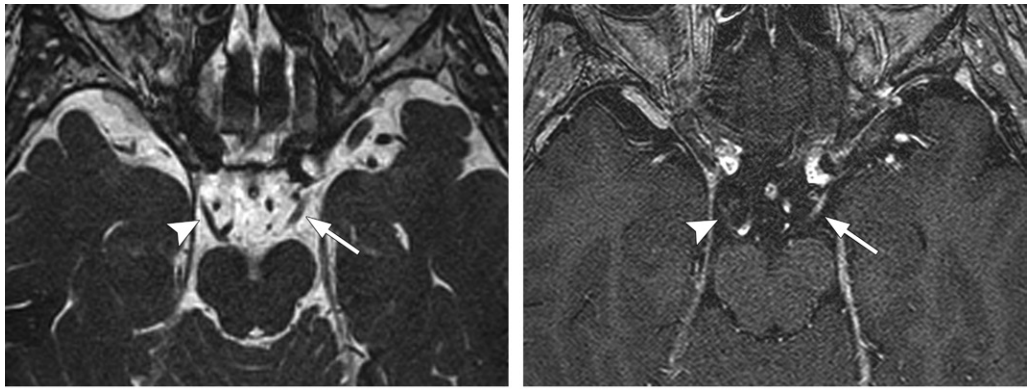

a. b.

Figure 13. Cranial neuropathy in a 72-year-old woman with diplopia and ptosis of the left eye. She underwent stereotactic radiosurgery for a left cavernous sinus meningioma 4 years earlier. **(a)** Axial fast imaging employing steady-state acquisition (FIESTA) image shows the cisternal portions of the left (arrow) and right (arrowhead) oculomotor nerves. **(b)** Axial contrast-enhanced T1-weighted image shows marked enhancement of the left oculomotor nerve (arrow), in contrast to that of the right oculomotor nerve (arrowhead).

as 1 year after completion of therapy, and the prevalence increases over time (81). As a result, patients who have undergone irradiation of the hypothalamus or pituitary region should undergo baseline endocrine evaluation within 1 year of completing irradiation, and regular testing is essential to achieve timely diagnosis and treatment.

The nature of radiation-induced damage to the hypothalamopituitary axis is not fully understood. However, direct neuronal damage by ionizing radiation with resulting degeneration and cell death, rather than vascular injury, is currently the preferred theory (83). Within the hypothalamopituitary axis, the growth hormone axis is the most vulnerable to radiation damage, followed by the gonadotropin, adrenocorticotropic hormone, and thyroid-stimulating hormone axes (81,83). Isolated growth hormone deficiency is the most frequent outcome after radiation doses of less than 40 Gy (81), whereas more intensive irradiation schedules—used in particular for those with nasopharyngeal carcinoma or skull base tumors—deliver a higher dose of radiation (≥60 Gy) and can lead to panhypopituitarism (83). Imaging may demonstrate varying degrees of atrophy of the pituitary gland, often in association with radiation-induced changes in adjacent structures such as leukoencephalopathy and internal carotid artery (ICA) stenosis (Fig 14).

Radiation-induced Brain Tumors

Cranial irradiation has been established as a cause of brain tumors, including meningiomas, gliomas, sarcomas, and nerve sheath tumors (84). As longer survival has been achieved with improvements in medical management of pri-

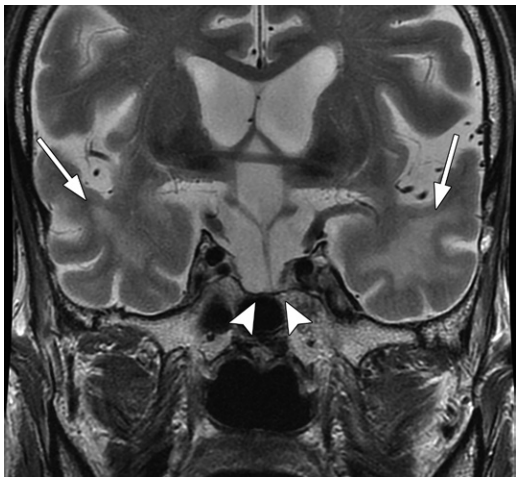

Figure 14. Atrophy of the pituitary gland and leukoencephalopathy in a 57-year-old man who underwent RT (standard-fractionation type) 30 years earlier for a pituitary adenoma. On a coronal T2-weighted image, the pituitary gland is markedly atrophic (arrowheads) and almost unidentifiable. The adjacent brain parenchyma (bilateral temporal lobes) is atrophic and exhibits hyperintense signal changes in the white matter (arrows), suggestive of radiation-induced leukoencephalopathy.

mary brain tumors, there is a higher incidence and a larger number of secondary tumors to deal with. Childhood or young adult cancer survivors who were exposed to cranial radiation have an increased risk of developing subsequent brain tumors compared with the general population (84).

Regarding the histotype, meningiomas are the most common subsequent brain tumors among aging adult survivors of childhood cancer who were exposed to cranial radiation (84). Although the absolute risk of radiation-induced meningiomas is not known, the latency period is more than 20 years in many cases (85). Long-term follow-up of epidemiologic studies revealed that the incidence continues to increase even after several decades and does not plateau over time (84). In a cohort of over 4000 childhood cancer survivors exposed to cranial radiation, the cumulative risk of subsequent meningioma was 5.6% by age 40 years (86). Cohort studies from the Childhood Cancer Survivor Study (86) and British Childhood Cancer Survivor Study (84) also demonstrated that the dose of radiation exposure to the cranium has a linear relationship with the risk of developing radiation-induced meningiomas.

The relationship between irradiation and induced meningiomas can be explained by the high sensitivity of the meninges to irradiation (85). Irradiation induces early meningeal reactions, including inflammatory adhesions between the brain and dura, leptomeningeal thickening, and stromal proliferation (85). Compared with spontaneous meningiomas, radiation-induced meningiomas have been reported to be associated with a higher number of calvarial tumors, multiple lesions, histologically atypical lesions, and aggressive biologic or clinical behavior in the course of the disease period (Fig 15) (85). Furthermore, higher doses of irradiation are associated with an increased risk of developing atypical/anaplastic or multiple meningiomas and a shorter latency period (85).

Fatty Marrow Changes of Spine

Histologically, two distinct phases of radiation-induced changes in the bone marrow—acute and chronic—have been described. In the acute phase, RT causes edema, vascular congestion, and capillary injury to the fine vasculature (87). In addition, dilatation of the sinusoids and hemorrhage in the irradiated bone marrow can be detected within the 1st week after RT (87). At imaging, these changes may be observed as increased signal intensity on short inversion time inversion-recovery (STIR) images (87). A transient increase in enhancement may also be observed during the acute phase (88).

In the chronic phase, hemopoietic cells and blood vessels are depleted and replaced by yellow fat cells, which can be observed as hyperintensity on T1-weighted images (Fig 16) (87). Signal intensity changes on T1-weighted images may begin to appear as early as 2 weeks after initiation of RT (88). T1-weighted images may demonstrate nonhomogeneous hyperintensity 3–6 weeks after initiation of RT and typical homogeneous hyperintensity 6–14 weeks after initiation of RT (87). Progressive and significant decreases in enhancement are also observed during the chronic phase (88), which may reflect chronic microvascular changes including arteriolocapillary occlusion and fibrosis.

Radiation-induced Osteonecrosis (Osteoradionecrosis) of Spine

Osteoradionecrosis (ORN) of the spine is a serious complication of RT for cancer treatment in which radiated bone becomes necrotic. Wong et al (89) defined ORN as slow-healing radiation-induced ischemic necrosis of bone associated with soft-tissue necrosis of variable extent occurring in the absence of local primary tumor necrosis, recurrence, or metastatic disease. ORN is most commonly found in the mandible after RT of head and neck cancer (89). ORN of the spine is rare, although it has been reported in the cervical (90,91) and lumbar (92) spine. In a retrospective review of 884 patients who underwent follow-up MRI after RT for nasopharyngeal cancer, ORN of the cervical spine was identified in nine patients (1%) (91).

Histopathologically, radiation produces a hypoxic, hypocellular, and hypovascular environment in which the basic metabolic demands for cellular survival cannot be met (89). Bone necrosis and

cartilage necrosis occur when radiation fibrosis and cellular injury limit the ability of tissues to adjust to normal wear and turnover, resulting in tissue breakdown (89). A contributory role of infection has been postulated in the development of ORN (91). The poorly vascularized necrotic tissue cannot resist infection well, which may result in secondary osteomyelitis and may be accompanied by fistula formation or cellulitis (89).

ORN of the spine can develop years after radiation exposure, and patients may present with pain and stiffness with or without neurologic symptoms (90–92). The bone destruction and hypoxic environment of ORN can result in spinal instability and a nidus for osteomyelitis. Infectious symptoms, such as fever and pus, soft-tissue swelling, and ulceration, may be noted (90,91).

CT images of ORN of the spine may demonstrate loss of the trabecular pattern, mixed osteolytic and osteosclerotic change, fractures, irregular endplate destruction, vertebral collapse, and spondylolisthesis (Fig 17) (90,92). At MRI, ORN of the spine typically exhibits hypointensity on T1-weighted images and enhancement (Fig 17) (90–92). Mixed signal intensity with both low- and high-signal-intensity foci may be observed on T2-weighted images (91). Adjacent soft tissue may appear edematous and exhibit enhancement (90,91).

ORN of the spine with or without osteomyelitis is often difficult to diagnose early because local-regional recurrence and bone metastasis have similar radiologic appearances (90,91). Wu et al (90) evaluated the MRI features of ORN and recurrent malignant disease of the upper cervical spine after irradiation for head and neck cancer. Several characteristic features of upper cervical ORN were proposed, including contiguous atlantoaxial or atlanto–occipital bone involvement with intervening joint space change, symmetric involvement of the bilateral aspects of the upper cervical spine, collapse of the vertebral body, reactive soft-tissue swelling, and ulceration of the posterior pharyngeal mucosa (90). ^{18}F–fluorodeoxyglucose (FDG) PET has limitations in distinguishing metastatic or recurrent lesions from ORN because the inflammatory response associated with ORN may be interpreted as false-positive strong uptake (90).

Radiation-induced Spinal Cord Myelopathy

Radiation-induced spinal cord myelopathy is a rare late delayed complication of radiation exposure to the spinal cord. Largely on the basis of clinical experience over many decades, most facilities limit the total dose to the spinal cord to less than 45–50 Gy in 1.8–2-Gy daily fractions (12,93,94). Radiation-induced spinal cord myelopathy has become a rare complication after conventional fractionated radiation treatment, and the risk of permanent injury is low (0.03%–0.2%) (93,94). However, cases of radiation-induced spinal cord myelopathy have reemerged with the increasing role of spine stereotactic RT and reirradiation (12,95,96). In addition, prior studies suggested that radiosensitizing systemic chemotherapy increases the risk of radiation-induced spinal cord myelopathy (93).

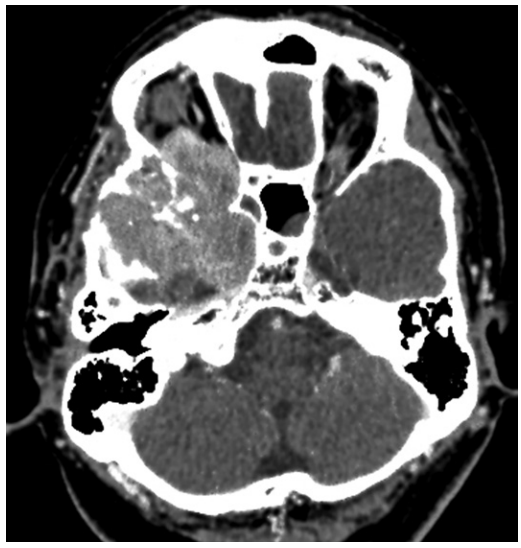

Figure 15. Atypical meningioma in a 47-year-old man with retinoblastoma who underwent enucleation of the left eye and RT (standard-fractionation type) of the right eye during childhood. Axial contrast-enhanced CT image shows a massive extra-axial tumor (atypical meningioma) in the right middle cranial fossa, extending into the right orbit and cavernous sinus with bone destruction.

The symptom onset of radiation-induced spinal cord myelopathy is most often insidious, and the latent period can range from a few months to several years after RT (95). The clinical manifestations of radiation-induced spinal cord myelopathy can be subtle initially, such as decreased temperature sensation or decreased proprioception. Symptoms may slowly progress to extremity weakness, Brown-Séquard syndrome, urinary or bowel incontinence, hyperreflexia, or complete paresis below the irradiated section of the spinal cord (12,95). Prior reports have suggested that radiation-induced spinal cord myelopathy is a progressive and permanent disease (12); however, clinical improvement has been noted (95).

Histopathologic changes of radiation-induced spinal cord myelopathy include demyelination, reactive gliosis and necrosis confined to white matter, and varying degrees of vascular changes in both white and gray matter (12). Radiation also stimulates astrocytes and microglial cells to produce cytokines, which increases the permeability of spinal cord blood vessels, leading to edema (12).

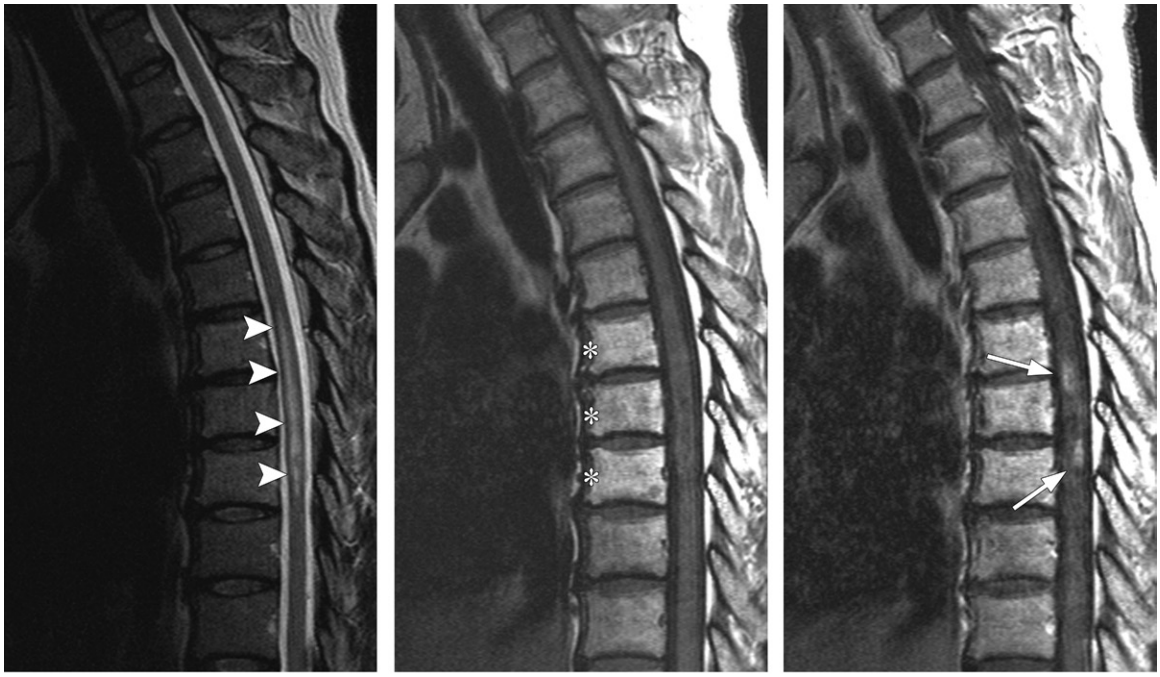

a. b. c.

Figure 16. Myelitis and fatty marrow changes in a 48-year-old woman with lower extremity weakness and paresthesia. She underwent RT (standard-fractionation type) 3 years earlier for a metastasis from lung cancer to T7. **(a)** Sagittal T2-weighted image shows longitudinal extensive myelitis as hyperintense signal changes (arrowheads). **(b)** Sagittal T1-weighted image shows fatty marrow changes of T5–T7 (*). **(c)** Sagittal contrast-enhanced T1-weighted image shows the myelitis seen in **a** as partial enhancement (arrows).

Characteristic MRI changes include spinal cord expansion and hyperintense signal changes on T2-weighted images (Fig 16) (12,95). T2 signal intensity abnormalities predominantly involve the central aspect of the spinal cord (95). Enhancement can be variable, reflecting inconsistencies and temporal variability in blood–spinal cord barrier permeability (Fig 16) (95). Much later, there may be atrophy without notable signal intensity abnormality (95). Hemorrhagic changes in the cord may be associated with severe cases (95).

MRI findings, including cord expansion and enhancement, are neither universally progressive nor permanent, and some radiologic and clinical improvement may occur during follow-up (95). According to Khan et al (95), clinical improvement may correlate well with radiologic improvement at longitudinal follow-up, and the mechanism of neurologic recovery may be due to resolution of cord edema and inflammation, remyelination, and revascularization. Previous reports suggested that some cases of radiation-induced spinal cord myelopathy are steroid responsive, and some patients may be treated using hyperbaric oxygen and bevacizumab (12).

Owing to its rarity, radiation-induced spinal cord myelopathy is often a diagnosis of exclusion. More common causes of transverse myelitis should be excluded before diagnosing radiation-induced spinal cord myelopathy, such as demyelinating diseases, rheumatoid diseases, infectious causes, vitamin B_{12} deficiency, and paraneoplastic syndromes. Although rare, recurrent or metastatic tumors should also be excluded in the context of a prior history of malignancy.

Prompt diagnosis of radiation-induced spinal cord myelopathy can be difficult because symptoms can vary, and MRI findings are nonspecific and can vary depending on the timing of MRI with respect to radiation exposure (95). Some imaging features may be useful in incorporating radiation-induced spinal cord myelopathy in the differential diagnosis, such as the longitudinally extensive cord signal intensity pattern corresponding to the radiation field and demonstration of T1-weighted hyperintense marrow signal changes in vertebrae included in the radiation field (Fig 16) (95).

Conclusion

The planning and delivery techniques of RT in the CNS have evolved substantially during the past few decades. However, the structures surrounding the target lesion are inevitably exposed to radiation, and a wide variety of radiation-induced changes may be observed at posttreatment imaging. Prompt diagnosis can be difficult because imaging findings of radiation-induced changes can be nonspecific, can vary depending on the timing of imaging with respect to radiation exposure, and may show significant overlap

a. b.

Figure 17. Osteoradionecrosis (ORN) of the spine in a 79-year-old woman with neck pain, ulceration of the posterior pharyngeal mucosa, and fever. She developed chronic nasopharyngitis after chemoradiation therapy (CRT) (standard-fractionation type) for malignant lymphoma of the oropharynx 9 years earlier. **(a)** Sagittal CT image (bone window) shows irregular endplate destruction and mild bone collapse of the upper cervical spine and C3-C4 spondylolisthesis. **(b)** Sagittal contrast-enhanced fat-saturated T1-weighted image shows enhancement of C2 and C3. Also noted are retropharyngeal edema and effusion at the posterior pharyngeal wall (arrows) and along the ventral portion of the cervical cord (arrowheads).

with those of tumor recurrence. Knowledge of the radiation treatment plan, amount of normal structures included, location of the target lesion, and amount of time elapsed since RT is markedly important at follow-up imaging. The reporting radiologist should be familiar with the timeline and expected imaging appearances after RT to avoid pitfalls in image interpretation.

References

1. Emami B, Lyman J, Brown A, et al. Tolerance of normal tissue to therapeutic irradiation. Int J Radiat Oncol Biol Phys 1991;21(1):109–122.
2. Stea B, Hazard LJ, Gonzalez VJ, Hamilton R. The role of radiation therapy in the control of locoregional and metastatic cancer. J Surg Oncol 2011;103(6):627–638.
3. Tofilon PJ, Fike JR. The radioresponse of the central nervous system: a dynamic process. Radiat Res 2000;153(4):357–370.
4. Nordal RA, Wong CS. Molecular targets in radiation-induced blood-brain barrier disruption. Int J Radiat Oncol Biol Phys 2005;62(1):279–287.
5. Roongpiboonsopit D, Kuijf HJ, Charidimou A, et al. Evolution of cerebral microbleeds after cranial irradiation in medulloblastoma patients. Neurology 2017;88(8):789–796.
6. Dietrich J, Monje M, Wefel J, Meyers C. Clinical patterns and biological correlates of cognitive dysfunction associated with cancer therapy. Oncologist 2008;13(12):1285–1295.
7. Brown JM, Carlson DJ, Brenner DJ. The tumor radiobiology of SRS and SBRT: are more than the 5 Rs involved? Int J Radiat Oncol Biol Phys 2014;88(2):254–262.
8. Steel GG, McMillan TJ, Peacock JH. The 5Rs of radiobiology. Int J Radiat Biol 1989;56(6):1045–1048.
9. Leksell L. The stereotaxic method and radiosurgery of the brain. Acta Chir Scand 1951;102(4):316–319.
10. Song CW, Glatstein E, Marks LB, et al. Biological Principles of Stereotactic Body Radiation Therapy (SBRT) and Stereotactic Radiation Surgery (SRS): Indirect Cell Death. Int J Radiat Oncol Biol Phys 2019. 10.1016/j.ijrobp.2019.02.047. Published online March 2, 2019.
11. Brandsma D, Stalpers L, Taal W, Sminia P, van den Bent MJ. Clinical features, mechanisms, and management of pseudoprogression in malignant gliomas. Lancet Oncol 2008;9(5):453–461.
12. Wong CS, Fehlings MG, Sahgal A. Pathobiology of radiation myelopathy and strategies to mitigate injury. Spinal Cord 2015;53(8):574–580.
13. Zhong X, Huang B, Feng J, Yang W, Liu H. Delayed leukoencephalopathy of non-small cell lung cancer patients with brain metastases underwent whole brain radiation therapy. J Neurooncol 2015;125(1):177–181.
14. Valk PE, Dillon WP. Radiation injury of the brain. AJNR Am J Neuroradiol 1991;12(1):45–62.
15. Brown PD, Gondi V, Pugh S, et al. Hippocampal Avoidance During Whole-Brain Radiotherapy Plus Memantine for Patients With Brain Metastases: Phase III Trial NRG Oncology CC001. J Clin Oncol 2020;38(10):1019–1029.
16. Oka M, Terae S, Kobayashi R, et al. MRI in methotrexate-related leukoencephalopathy: disseminated necrotising leukoencephalopathy in comparison with mild leukoencephalopathy. Neuroradiology 2003;45(7):493–497.
17. Pande AR, Ando K, Ishikura R, et al. Disseminated necrotizing leukoencephalopathy following chemoradiation therapy for acute lymphoblastic leukemia. Radiat Med 2006;24(7):515–519.
18. Kim JY, Kim ST, Nam DH, Lee JI, Park K, Kong DS. Leukoencephalopathy and disseminated necrotizing leukoencephalopathy following intrathecal methotrexate chemotherapy and radiation therapy for central nerve system lymphoma or leukemia. J Korean Neurosurg Soc 2011;50(4):304–310.
19. Kumar AJ, Leeds NE, Fuller GN, et al. Malignant gliomas: MR imaging spectrum of radiation therapy– and chemotherapy-induced necrosis of the brain after treatment. Radiology 2000;217(2):377–384.
20. Wang YX, King AD, Zhou H, et al. Evolution of radiation-induced brain injury: MR imaging–based study. Radiology 2010;254(1):210–218.
21. Shah R, Vattoth S, Jacob R, et al. Radiation necrosis in the brain: imaging features and differentiation from tumor recurrence. RadioGraphics 2012;32(5):1343–1359.
22. Ruben JD, Dally M, Bailey M, Smith R, McLean CA, Fedele P. Cerebral radiation necrosis: incidence, outcomes, and risk

factors with emphasis on radiation parameters and chemotherapy. Int J Radiat Oncol Biol Phys 2006;65(2):499–508.
23. Galldiks N, Kocher M, Ceccon G, et al. Imaging challenges of immunotherapy and targeted therapy in patients with brain metastases: response, progression, and pseudoprogression. Neuro Oncol 2020;22(1):17–30.
24. Deibert CP, Ahluwalia MS, Sheehan JP, et al. Bevacizumab for refractory adverse radiation effects after stereotactic radiosurgery. J Neurooncol 2013;115(2):217–223.
25. Mullins ME, Barest GD, Schaefer PW, Hochberg FH, Gonzalez RG, Lev MH. Radiation necrosis versus glioma recurrence: conventional MR imaging clues to diagnosis. AJNR Am J Neuroradiol 2005;26(8):1967–1972.
26. Wang J, Miao Y, Ou X, et al. Development and validation of a model for temporal lobe necrosis for nasopharyngeal carcinoma patients with intensity modulated radiation therapy. Radiat Oncol 2019;14(1):42.
27. Lee AW, Kwong DL, Leung SF, et al. Factors affecting risk of symptomatic temporal lobe necrosis: significance of fractional dose and treatment time. Int J Radiat Oncol Biol Phys 2002;53(1):75–85.
28. Asao C, Korogi Y, Kitajima M, et al. Diffusion-weighted imaging of radiation-induced brain injury for differentiation from tumor recurrence. AJNR Am J Neuroradiol 2005;26(6):1455–1460.
29. Hein PA, Eskey CJ, Dunn JF, Hug EB. Diffusion-weighted imaging in the follow-up of treated high-grade gliomas: tumor recurrence versus radiation injury. AJNR Am J Neuroradiol 2004;25(2):201–209.
30. van Dijken BRJ, van Laar PJ, Holtman GA, van der Hoorn A. Diagnostic accuracy of magnetic resonance imaging techniques for treatment response evaluation in patients with high-grade glioma: a systematic review and meta-analysis. Eur Radiol 2017;27(10):4129–4144.
31. Kazda T, Bulik M, Pospisil P, et al. Advanced MRI increases the diagnostic accuracy of recurrent glioblastoma: single institution thresholds and validation of MR spectroscopy and diffusion weighted MR imaging. Neuroimage Clin 2016;11:316–321.
32. Sundgren PC. MR spectroscopy in radiation injury. AJNR Am J Neuroradiol 2009;30(8):1469–1476.
33. Zhang H, Ma L, Wang Q, Zheng X, Wu C, Xu BN. Role of magnetic resonance spectroscopy for the differentiation of recurrent glioma from radiation necrosis: a systematic review and meta-analysis. Eur J Radiol 2014;83(12):2181–2189.
34. Sugahara T, Korogi Y, Tomiguchi S, et al. Posttherapeutic intraaxial brain tumor: the value of perfusion-sensitive contrast-enhanced MR imaging for differentiating tumor recurrence from nonneoplastic contrast-enhancing tissue. AJNR Am J Neuroradiol 2000;21(5):901–909.
35. Barajas RF Jr, Chang JS, Segal MR, et al. Differentiation of recurrent glioblastoma multiforme from radiation necrosis after external beam radiation therapy with dynamic susceptibility-weighted contrast-enhanced perfusion MR imaging. Radiology 2009;253(2):486–496.
36. Zakhari N, Taccone MS, Torres CH, et al. Prospective comparative diagnostic accuracy evaluation of dynamic contrast-enhanced (DCE) vs. dynamic susceptibility contrast (DSC) MR perfusion in differentiating tumor recurrence from radiation necrosis in treated high-grade gliomas. J Magn Reson Imaging 2019;50(2):573–582.
37. Seeger A, Braun C, Skardelly M, et al. Comparison of three different MR perfusion techniques and MR spectroscopy for multiparametric assessment in distinguishing recurrent high-grade gliomas from stable disease. Acad Radiol 2013;20(12):1557–1565.
38. Grade M, Hernandez Tamames JA, Pizzini FB, Achten E, Golay X, Smits M. A neuroradiologist's guide to arterial spin labeling MRI in clinical practice. Neuroradiology 2015;57(12):1181–1202.
39. Ye J, Bhagat SK, Li H, et al. Differentiation between recurrent gliomas and radiation necrosis using arterial spin labeling perfusion imaging. Exp Ther Med 2016;11(6):2432–2436.
40. Ricci PE, Karis JP, Heiserman JE, Fram EK, Bice AN, Drayer BP. Differentiating recurrent tumor from radiation necrosis: time for re-evaluation of positron emission tomography? AJNR Am J Neuroradiol 1998;19(3):407–413.
41. Glaudemans AW, Enting RH, Heesters MA, et al. Value of 11C-methionine PET in imaging brain tumours and metastases. Eur J Nucl Med Mol Imaging 2013;40(4):615–635.
42. Brandes AA, Franceschi E, Tosoni A, et al. MGMT promoter methylation status can predict the incidence and outcome of pseudoprogression after concomitant radiochemotherapy in newly diagnosed glioblastoma patients. J Clin Oncol 2008;26(13):2192–2197.
43. Taal W, Brandsma D, de Bruin HG, et al. Incidence of early pseudo-progression in a cohort of malignant glioma patients treated with chemoirradiation with temozolomide. Cancer 2008;113(2):405–410.
44. Tsien C, Galbán CJ, Chenevert TL, et al. Parametric response map as an imaging biomarker to distinguish progression from pseudoprogression in high-grade glioma. J Clin Oncol 2010;28(13):2293–2299.
45. Young RJ, Gupta A, Shah AD, et al. Potential utility of conventional MRI signs in diagnosing pseudoprogression in glioblastoma. Neurology 2011;76(22):1918–1924.
46. Rowe LS, Butman JA, Mackey M, et al. Differentiating pseudoprogression from true progression: analysis of radiographic, biologic, and clinical clues in GBM. J Neurooncol 2018;139(1):145–152.
47. Kong DS, Kim ST, Kim EH, et al. Diagnostic dilemma of pseudoprogression in the treatment of newly diagnosed glioblastomas: the role of assessing relative cerebral blood flow volume and oxygen-6-methylguanine-DNA methyltransferase promoter methylation status. AJNR Am J Neuroradiol 2011;32(2):382–387.
48. Prager AJ, Martinez N, Beal K, Omuro A, Zhang Z, Young RJ. Diffusion and perfusion MRI to differentiate treatment-related changes including pseudoprogression from recurrent tumors in high-grade gliomas with histopathologic evidence. AJNR Am J Neuroradiol 2015;36(5):877–885.
49. Thomas AA, Arevalo-Perez J, Kaley T, et al. Dynamic contrast enhanced T1 MRI perfusion differentiates pseudoprogression from recurrent glioblastoma. J Neurooncol 2015;125(1):183–190.
50. Choi YJ, Kim HS, Jahng GH, Kim SJ, Suh DC. Pseudoprogression in patients with glioblastoma: added value of arterial spin labeling to dynamic susceptibility contrast perfusion MR imaging. Acta Radiol 2013;54(4):448–454.
51. Thust SC, van den Bent MJ, Smits M. Pseudoprogression of brain tumors. J Magn Reson Imaging 2018;48(3):571–589.
52. Hygino da Cruz LC Jr, Rodriguez I, Domingues RC, Gasparetto EL, Sorensen AG. Pseudoprogression and pseudoresponse: imaging challenges in the assessment of posttreatment glioma. AJNR Am J Neuroradiol 2011;32(11):1978–1985.
53. van den Bent MJ, Klein M, Smits M, et al. Bevacizumab and temozolomide in patients with first recurrence of WHO grade II and III glioma, without 1p/19q co-deletion (TAVAREC): a randomised controlled phase 2 EORTC trial. Lancet Oncol 2018;19(9):1170–1179.
54. Wen PY, Macdonald DR, Reardon DA, et al. Updated response assessment criteria for high-grade gliomas: Response Assessment in Neuro-oncology Working Group. J Clin Oncol 2010;28(11):1963–1972.
55. Farid N, Almeida-Freitas DB, White NS, et al. Combining diffusion and perfusion differentiates tumor from bevacizumab-related imaging abnormality (BRIA). J Neurooncol 2014;120(3):539–546.
56. Ratai EM, Zhang Z, Snyder BS, et al. Magnetic resonance spectroscopy as an early indicator of response to anti-angiogenic therapy in patients with recurrent glioblastoma: RTOG 0625/ACRIN 6677. Neuro Oncol 2013;15(7):936–944.
57. Bitzer M, Topka H. Progressive cerebral occlusive disease after radiation therapy. Stroke 1995;26(1):131–136.
58. Kralik SF, Watson GA, Shih CS, Ho CY, Finke W, Buchsbaum J. Radiation-Induced Large Vessel Cerebral Vasculopathy in Pediatric Patients With Brain Tumors Treated With Proton Radiation Therapy. Int J Radiat Oncol Biol Phys 2017;99(4):817–824.

59. Ullrich NJ, Robertson R, Kinnamon DD, et al. Moyamoya following cranial irradiation for primary brain tumors in children. Neurology 2007;68(12):932–938.
60. Omura M, Aida N, Sekido K, Kakehi M, Matsubara S. Large intracranial vessel occlusive vasculopathy after radiation therapy in children: clinical features and usefulness of magnetic resonance imaging. Int J Radiat Oncol Biol Phys 1997;38(2):241–249.
61. Aoki S, Hayashi N, Abe O, et al. Radiation-induced arteritis: thickened wall with prominent enhancement on cranial MR images—report of five cases and comparison with 18 cases of moyamoya disease. Radiology 2002;223(3):683–688.
62. Nanney AD 3rd, El Tecle NE, El Ahmadieh TY, et al. Intracranial aneurysms in previously irradiated fields: literature review and case report. World Neurosurg 2014;81(3-4):511–519.
63. Cutsforth-Gregory JK, Lanzino G, Link MJ, Brown RD Jr, Flemming KD. Characterization of radiation-induced cavernous malformations and comparison with a non-radiation cavernous malformation cohort. J Neurosurg 2015;122(5):1214–1222.
64. Nagy G, McCutcheon BA, Giannini C, Link MJ, Pollock BE. Radiation-Induced Cavernous Malformations After Single-Fraction Meningioma Radiosurgery. Oper Neurosurg (Hagerstown) 2018;15(2):207–212.
65. Heckl S, Aschoff A, Kunze S. Radiation-induced cavernous hemangiomas of the brain: a late effect predominantly in children. Cancer 2002;94(12):3285–3291.
66. Khasminsky V, Yalon M, Greenberg G, Tsarfaty G, Atar E, Hoffmann C. Detection of cavernous malformations after whole-brain radiotherapy in primitive neuroectodermal tumor patients: comparing susceptibility-weighted imaging and T2 gradient-echo sequences. Neuroradiology 2018;60(9):913–919.
67. Black DF, Morris JM, Lindell EP, et al. Stroke-like migraine attacks after radiation therapy (SMART) syndrome is not always completely reversible: a case series. AJNR Am J Neuroradiol 2013;34(12):2298–2303.
68. Khanipour Roshan S, Salmela MB, McKinney AM. Susceptibility-weighted imaging in stroke-like migraine attacks after radiation therapy syndrome. Neuroradiology 2015;57(11):1103–1109.
69. Kerklaan JP, Lycklama á Nijeholt GJ, Wiggenraad RG, Berghuis B, Postma TJ, Taphoorn MJ. SMART syndrome: a late reversible complication after radiation therapy for brain tumours. J Neurol 2011;258(6):1098–1104.
70. Shanley DJ. Mineralizing microangiopathy: CT and MRI. Neuroradiology 1995;37(4):331–333.
71. Price RA, Birdwell DA. The central nervous system in childhood leukemia. III. Mineralizing microangiopathy and dystrophic calcification. Cancer 1978;42(2):717–728.
72. Shuto T, Ohtake M, Matsunaga S. Proposed mechanism for cyst formation and enlargement following gamma knife surgery for arteriovenous malformations. J Neurosurg 2012;117(Special_Suppl,Suppl):135–143.
73. Hasegawa T, Kato T, Naito T, et al. Long-Term Outcomes for Pediatric Patients with Brain Arteriovenous Malformations Treated with Gamma Knife Radiosurgery. II. The Incidence of Cyst Formation, Encapsulated Hematoma, and Radiation-Induced Tumor. World Neurosurg 2019;126:e1526–e1536.
74. Archer EL, Liao EA, Trobe JD. Radiation-Induced Optic Neuropathy: Clinical and Imaging Profile of Twelve Patients. J Neuroophthalmol 2019;39(2):170–180.
75. Vaphiades MS, Spencer SA, Riley K, Francis C, Deitz L, Kline LB. Radiation-induced ocular motor cranial nerve palsies in patients with pituitary tumor. J Neuroophthalmol 2011;31(3):210–213.
76. Tishler RB, Loeffler JS, Lunsford LD, et al. Tolerance of cranial nerves of the cavernous sinus to radiosurgery. Int J Radiat Oncol Biol Phys 1993;27(2):215–221.
77. Alberico RA, Fenstermaker RA, Lobel J. Focal enhancement of cranial nerve V after radiosurgery with the Leksell gamma knife: experience in 15 patients with medically refractory trigeminal neuralgia. AJNR Am J Neuroradiol 2001;22(10):1944–1948.
78. Kong L, Lu JJ, Liss AL, et al. Radiation-induced cranial nerve palsy: a cross-sectional study of nasopharyngeal cancer patients after definitive radiotherapy. Int J Radiat Oncol Biol Phys 2011;79(5):1421–1427.
79. Saremi F, Helmy M, Farzin S, Zee CS, Go JL. MRI of cranial nerve enhancement. AJR Am J Roentgenol 2005;185(6):1487–1497.
80. Crush AB, Howe BM, Spinner RJ, et al. Malignant involvement of the peripheral nervous system in patients with cancer: multimodality imaging and pathologic correlation. RadioGraphics 2014;34(7):1987–2007.
81. Darzy KH, Shalet SM. Hypopituitarism as a consequence of brain tumours and radiotherapy. Pituitary 2005;8(3-4):203–211.
82. Appelman-Dijkstra NM, Kokshoorn NE, Dekkers OM, et al. Pituitary dysfunction in adult patients after cranial radiotherapy: systematic review and meta-analysis. J Clin Endocrinol Metab 2011;96(8):2330–2340.
83. Pai HH, Thornton A, Katznelson L, et al. Hypothalamic/pituitary function following high-dose conformal radiotherapy to the base of skull: demonstration of a dose-effect relationship using dose-volume histogram analysis. Int J Radiat Oncol Biol Phys 2001;49(4):1079–1092.
84. Taylor AJ, Little MP, Winter DL, et al. Population-based risks of CNS tumors in survivors of childhood cancer: the British Childhood Cancer Survivor Study. J Clin Oncol 2010;28(36):5287–5293.
85. Yamanaka R, Hayano A, Kanayama T. Radiation-Induced Meningiomas: An Exhaustive Review of the Literature. World Neurosurg 2017;97:635–644.e8.
86. Bowers DC, Moskowitz CS, Chou JF, et al. Morbidity and Mortality Associated With Meningioma After Cranial Radiotherapy: A Report From the Childhood Cancer Survivor Study. J Clin Oncol 2017;35(14):1570–1576.
87. Stevens SK, Moore SG, Kaplan ID. Early and late bone-marrow changes after irradiation: MR evaluation. AJR Am J Roentgenol 1990;154(4):745–750.
88. Otake S, Mayr NA, Ueda T, Magnotta VA, Yuh WT. Radiation-induced changes in MR signal intensity and contrast enhancement of lumbosacral vertebrae: do changes occur only inside the radiation therapy field? Radiology 2002;222(1):179–183.
89. Wong JK, Wood RE, McLean M. Conservative management of osteoradionecrosis. Oral Surg Oral Med Oral Pathol Oral Radiol Endod 1997;84(1):16–21.
90. Wu LA, Liu HM, Wang CW, Chen YF, Hong RL, Ko JY. Osteoradionecrosis of the upper cervical spine after radiation therapy for head and neck cancer: differentiation from recurrent or metastatic disease with MR imaging. Radiology 2012;264(1):136–145.
91. King AD, Griffith JF, Abrigo JM, et al. Osteoradionecrosis of the upper cervical spine: MR imaging following radiotherapy for nasopharyngeal carcinoma. Eur J Radiol 2010;73(3):629–635.
92. Rolton DJ, Blagg SE, Hughes RJ. Osteoradionecrosis of the lumbar spine 25 years after radiotherapy. J Bone Joint Surg Br 2011;93(9):1279–1281.
93. Schultheiss TE. The radiation dose-response of the human spinal cord. Int J Radiat Oncol Biol Phys 2008;71(5):1455–1459.
94. Kirkpatrick JP, van der Kogel AJ, Schultheiss TE. Radiation dose-volume effects in the spinal cord. Int J Radiat Oncol Biol Phys 2010;76(3,suppl):S42–S49.
95. Khan M, Ambady P, Kimbrough D, et al. Radiation-Induced Myelitis: Initial and Follow-Up MRI and Clinical Features in Patients at a Single Tertiary Care Institution during 20 Years. AJNR Am J Neuroradiol 2018;39(8):1576–1581.
96. Sahgal A, Chang JH, Ma L, et al. Spinal Cord Dose Tolerance to Stereotactic Body Radiation Therapy. Int J Radiat Oncol Biol Phys 2019. 10.1016/j.ijrobp.2019.09.038. Published online October 10, 2019.